Nanoscopic dopamine transporter distribution and conformation are inversely regulated by excitatory drive and D_2-autoreceptor activity

Matthew D. Lycas[1], Aske L. Ejdrup[1], Andreas T. Sørensen[1], Nicolai O. Haahr[1], Søren H. Jørgensen[1], Daryl A. Guthrie [2], Jonatan F. Støier[1], Christian Werner[3], Amy Hauck Newman[2], Markus Sauer[3], Freja Herborg[1] and Ulrik Gether[1*]

[1]Molecular Neuropharmacology and Genetics Laboratory, Department of Neuroscience, Faculty of Health and Medical Sciences, Maersk Tower 7.5, University of Copenhagen, DK-2200 Copenhagen, Denmark

[2]Medicinal Chemistry Section, Molecular Targets and Medications Discovery Branch, National Institute on Drug Abuse-Intramural Research Program, National Institutes of Health, Baltimore, Maryland 21224

[3]Department of Biotechnology and Biophysics, Biocenter, Julius-Maximilians-Universität Würzburg, Am Hubland, 97074 Würzburg, Germany

*Correspondence: gether@sund.ku.dk

Abstract

The nanoscopic organization and regulation of individual molecular components in presynaptic varicosities of neurons releasing modulatory volume neurotransmitters like dopamine (DA) remain largely elusive. Here we show by application of several single-molecule sensitive super-resolution microscopy techniques to cultured neurons and mouse striatal slices, that the dopamine transporter (DAT), a key protein in varicosities of dopaminergic neurons, exists in the membrane in dynamic equilibrium between an inward-facing nanodomain-localized and outward-facing unclustered configuration. The balance between these configurations is inversely regulated by excitatory drive and by DA D2-autoreceptor activation in a manner dependent on Ca^{2+}-influx via N-type voltage-gated Ca^{2+}-channels. The DAT nanodomains contain tens of transporters molecules and overlap with nanodomains of PIP2 (phosphatidylinositol-4,5-bisphosphate) but show little overlap with D2-autoreceptor, syntaxin-1 and clathrin nanodomains. Summarized, the data reveal a mechanism for rapid alterations in nanoscopic DAT distribution and show a striking link of this to the conformational state of the transporter.

19 **Introduction**

20 In its 15 years of utilization, super-resolution microscopy has improved our insights into the molecular
21 organization and dynamic regulation of pre- and postsynaptic structures in the brain. Indeed, it has
22 become clear that regulatory processes of fundamental importance for spatial and temporal control of
23 synaptic signaling occur at a nanoscale level. In excitatory synapses, for example, it is now believed that
24 AMPA-type and NMDA-type ionotropic glutamate receptors segregate into distinct nanodomains in the
25 postsynaptic density and that this co-organization plays a critical role in synaptic physiology[1,2]. Such
26 studies highlight the importance of observing past the diffraction limit of visible light while still leveraging
27 labeling strategies and live imaging compatibility that light microscopy provides[1-3].

28 Much less is known about the nanoscale architecture of the presynaptic compartment in neurons
29 releasing modulatory transmitters like dopamine (DA). DA neurons project from the midbrain to the basal
30 ganglia, the limbic system and the prefrontal cortex to mediate the role of DA in motor functions, reward
31 mechanisms and learning processes[4,5]. The DA neurons have remarkable axonal arbors with numerous
32 release sites (i.e. varicosities) that enable single DA neurons to affect the function of multiple target
33 neurons[6,7]. DA neurotransmission, however, differs from classical fast synaptic transmission by operating
34 perhaps primarily via "volume transmission", that is, DA is predominantly released from non-synaptic
35 release sites to act on target cells often located microns away[6,8]. It remains nonetheless elusive how the
36 different molecular components in the dopaminergic release sites need to be organized at a nanoscale
37 level and individually regulated to enable proper neurotransmitter release and reuptake.

38 A key regulator of DA neurotransmission, the dopamine transporter (DAT), is highly expressed in
39 the varicosities of DA neurons and removes released DA from the extracellular space. DAT has received
40 attention as the primary target for therapeutics, such as methylphenidate, and drugs of abuse such as
41 methamphetamine and cocaine[9,10]. Not surprisingly, DAT is subject to tight regulation through several
42 mechanisms involving post-translational modifications, protein-protein interactions and protein-lipid

43 interactions[9,11,12]. Moreover, we recently showed by application of super-resolution imaging that DAT
44 regulation might involve mechanisms that cannot be revealed by more classical methods[13]. Our data
45 showed that DAT localizes to discrete nanodomains in the plasma membrane of cultured DA neurons and
46 that activation of NMDA-receptors reduced DAT nanodomain localization[13]. Although this indicated that
47 nanoscale dynamics in dopamine varicosities could be critical for controlling DA neurotransmission, the
48 mechanisms and functional implications remain unknown.

49 Here we use several super-resolution imaging techniques, including Photoactivated Localization
50 Microscopy (PALM)[14], direct Stochastic Optical Reconstruction Microscopy (dSTORM)[15,16], 10 x Expansion
51 Microscopy (ExM)[17-19] and single-particle tracking dSTORM (spt-dSTORM)[20] together with new fluorescent
52 cocaine-analogues[21] and new data analysis tools, to investigate how DAT and associated molecular
53 components at DA varicosities are dynamically regulated. In summary, our experimental efforts
54 demonstrate that excitatory drive and D2-autoreceptor activity inversely regulate in a Ca^{2+} dependent
55 manner the conformational state of DAT and its localization in DA varicosities to PIP2 enriched
56 nanodomains separate from syntaxin-1 (STX-1), D2-autoreceptor or clathrin nanodomains. In this way,
57 our study uncovers a hitherto unknown level of regulation of an essential membrane protein in a
58 modulatory transmitter terminal.

59

60

61 **Results**

62 **DAT shows nanodomain distribution in cultured neurons and striatal slices.** There are a variety of
63 strategies to resolve biological structures past the diffraction limit of light, but each method is associated
64 with strengths, compromises, and potential artefacts. Our previous dSTORM work suggested that DAT
65 distributes into nanodomains at DA varicosities of cultured midbrain DA neurons[13]. To substantiate this
66 finding, we decided to assess DAT distribution across a variety of super resolution methods and to
67 ultimately investigate whether DAT is distributed into nanodomains in intact tissue. First, we assessed the
68 distribution of DAT regardless of potential antibody-induced clustering artifacts by transfecting cultured
69 DA neurons with DAT having the photoconvertible fluorescent protein mEOS2[22] fused to the N-terminus.
70 Images of tyrosine hydroxylase (TH) positive varicosities revealed a clustered distribution of the mEOS2-
71 DAT signal surrounding the cytosolic TH signal (Fig. 1A-D), similar to that seen by imaging the endogenous
72 DAT by dSTORM[13]. We next employed astigmatic 3D-dSTORM to show that the DAT nanodomains were
73 localized to the periphery of the varicosities, substantiating that DAT is found mainly in the plasma
74 membrane (Fig. 1E-H). To assess the distribution of DAT in intact tissue, we analyzed coronal mouse brain
75 slices (Fig. 1I-L). Widefield imaging exposed the DAT positive varicosities and by dSTORM we could
76 visualize DAT in single varicosities, showing a nanodomain distribution like that seen in cultured neurons
77 (Fig. 1I-L). To exclude that the observed distribution of DAT was not caused by artifacts introduced by the
78 single molecule localization microscopy approach (e.g., "overcounting" [23]), we turned to ExM where
79 nanoscale spatial resolution is obtained by expanding the tissue sample using a polymer system[19]. We
80 employed a 10x expansion protocol[18] to mouse striatal slices before DAT imaging using a spinning disk
81 confocal microscope (Fig. 1M-P). In the stained expanded sample, we captured the intermingled axonal
82 network of DA neurons while at the same time observing clustering of DAT into nanodomains in
83 varicosities (Fig. 1M-P). Summarized, the distribution of DAT into nanodomains in the plasma membrane
84 of DA neurons was substantiated by several high-resolution imaging techniques.

85 Having reaffirmed the clustered organization of DAT with different techniques and in intact brain
86 tissue, we decided to focus on the dSTORM technology in our subsequent studies because of its
87 quantitative nature and single-molecule sensitivity. To derive quantitative measures for the clustered
88 distribution of DAT , we employed the DBSCAN algorithm (density based spatial clustering of applications
89 with noise)[13,24] and extracted two key parameters from the analysis: the size of the nanoclusters and the
90 density of localizations within the clusters (Fig. 1Q-S). The size was quantified as the fraction of clusters
91 with a diameter >75 nm (Fig. 1R). This size was chosen as threshold to exclude any clusters that might be
92 the result of amplified labeling of single proteins and thus might arise from the antibody labeling
93 methodology. By assessing the density of localizations as well, we could determine changes in the number
94 of molecules in a cluster without a change in cluster size. Dense clusters were defined as clusters with >80
95 localizations within a radius of 50 nm (dense clusters in red) (Fig. 1S). We also employed Voronoi
96 tessellation to compare localization density distributions in a parameter free fashion [25]. In this use of
97 Voronoi tessellation, clusters themselves were not identified but localization density changes could be
98 detected with greater sensitivity (Fig. 1T).

99 We also wanted to estimate how many DAT molecules are present in an average DAT nanodomain
100 defined by the DBSCAN analysis. We used a protocol modified from[26,27] and labeled cultured DA neurons
101 with sequential dilutions of the primary DAT antibody. This enabled us to define that a minimum cluster
102 is made from ~three localizations and that an average large cluster contains ~33 copies of the antibody
103 corresponding to 50-100 DAT molecules as a rough estimate (Supplementary Fig. 1). The same data series
104 lent itself perfectly for cluster analysis by varied label density cluster verification, enabling us to
105 distinguish between random clustering arising from multiple observations of single fluorophores and true
106 clustering[28]. In agreement with our data in DAT expressing Cath.a-differentiated (CAD) cells[13], our analysis
107 supported that the clustering behavior of DAT in cultured neurons reflect true nanocluster formation
108 (Supplementary Fig. 2).

109

110 **Nanodomain localized DAT is preferentially in an inward-facing conformation.** To assess putative
111 functional implications of the nanoclustered distribution of DAT, we investigated whether this could
112 involve a conformational bias with nanoclustered DAT having a different conformation than unclustered
113 DAT. Cocaine and cocaine-like inhibitors are known to bind with higher affinity to DAT in the outward-
114 facing conformation than in the inward-facing conformation[29,30]. We envisioned accordingly (and in line
115 with[31]) that an indirect measure of the conformational state of DAT inside and outside the nanodomains
116 could be obtained by parallel imaging of binding to DAT of a fluorescently tagged cocaine-analogue and
117 of DAT itself; that is, as a result of its conformational bias the cocaine-analogue would be expected to
118 bind more to outward-facing than to inward-facing transporters at a subsaturating concentration. We
119 labeled cultured DA neurons and mEOS2-DAT expressing CAD cells with DG3-63 (10 nM), an analogue of
120 cocaine tagged with JF_{646} suited for dSTORM (Fig. 2A-D). The DG3-63 signal generally appeared somewhat
121 less clustered as compared to that observed by our other approaches (see Fig. 1). This might indicate a
122 preferential binding of DG3-63 to unclustered DAT, which was supported by dual-color images of DG3-63
123 labelled DAT and mEOS-DAT, showing a more dispersed DG3-63 signal as compared to a more clustered
124 mEOS2-DAT signal (Fig. 2E-G). Importantly, the DG3-63 signal was specific as it was essentially eliminated
125 by excess of unlabeled cocaine (Fig. 2H). To quantify whether DG3-63 preferentially bound to unclustered
126 DAT, we used a modification of the principles outlined by the colocalization extension of the Voronoi
127 tessellation algorithm [25] where associated DG3-63 was identified by including DG3-63 localizations within
128 25 nm from an mEOS2-DAT localization (Fig. 2I-K). The total mEOS2-DAT Voronoi tessellated area
129 distribution showed a preference for smaller tessellated areas consistent with a clustered distribution
130 (Fig. 2L). In contrast, the mEOS2-DAT-associated DG3-63 localizations resided on larger Voronoi
131 tessellated areas; hence, DG3-63 binding was not enriched in the DAT nanodomains containing the
132 highest density of DAT molecules (Fig. 2L). This suggests that nanoclustered DAT are less prone to bind

133 DG3-63, consistent with a more inward-facing transporter conformation or a less accessible binding site.
134 Interestingly, by analyzing the distribution of mEOS2-DAT after treatment with an excess, and thereby
135 saturating concentration, of cocaine, we observed a dispersal of the signal. This supports that forcing the
136 transporter into an outward-facing conformation may release the transporter from the nanodomains
137 (Supplementary Fig. 3).

138 We further rationalized that if the nanoscale DAT distribution reflects its molecular conformation,
139 then a redistribution would be expected for a DAT variant with a conformational bias. Accordingly, we
140 compared in transfected CAD cells clustering of WT DAT with that of a disease-associated DAT mutation
141 (D421N) known to be shifted towards an inward-facing conformation[32] (Fig. 2M-R). In agreement with the
142 idea that inward-facing DAT will display preferential localization to nanodomains, dSTORM after
143 immunolabeling revealed for D421N compared to WT both a higher fraction of large clusters (diameter
144 >75 nm) and a higher fraction of localizations in dense clusters (Fig. 2N, O, Q, R) without a change in total
145 number of detected localizations (Fig. 2P). Summarized, the data support that DAT preferentially assumes
146 an inward-facing conformation in DAT nanodomains while the conformation outside the nanodomains
147 conceivably is more outward-facing.

148

149 **NMDA receptor activation declusters DAT in striatal slices.** We next assessed whether DAT nanodomain
150 distribution was sensitive to NMDA stimulation in intact tissue (Fig. 2I-P) as we previously observed in
151 cultured neurons[13]. Notably, NMDA receptors are present in DA terminals where they can stimulate DA
152 release[33]. Acute coronal striatal slices were treated for 5 min with vehicle, NMDA or NMDA plus the NMDA
153 receptor antagonist (2R)-amino-5-phosphonovaleric acid (AP5) before DAT immunolabeling and dSTORM
154 (Fig. 3A). Because each dSTORM image contained a vast number of DAT positive varicosities, we
155 developed a new collection algorithm for automated and unbiased isolation of these varicosities, allowing
156 subsequent quantification of DAT clustering (Fig. 3B, C). Following NMDA treatment, both the fraction of

157 clusters >75 nm and the faction of localizations in dense clusters decreased; an effect that was muted by
158 the NMDA antagonist AP5 (Fig. 3D, E). Note that the comparisons were normalized to the control sample
159 from the individual imaging session to correct for unavoidable variability in sample preparations and
160 between imaging sessions. Importantly, the data were further supported by Voronoi tessellation showing
161 that NMDA, but not NMDA + AP5, reduced the fraction of smaller tessellated areas and thus clustering
162 (Fig. 3F). We conclude that local activation of NMDA receptors in intact tissue promotes dispersal of DAT
163 nanodomains.
164
165 **DAT nanodomain localization is regulated by neuronal activity.** We speculated whether persistent
166 changes in membrane potential and thereby in neuronal excitability would affect DAT nanodomain
167 distribution. To test this, we expressed the bacterial sodium channel (mNaChBac) or the inward-rectifier
168 potassium channel (Kir2.1)[34,35] in cultured DA neurons to make them more or less excitable, respectively
169 [34]. In agreement with selective expression in DA neurons, we confirmed that transduced cells were also
170 DAT positive (Supplementary Fig. 4). Electrophysiological recordings on single neurons showed that the
171 pacemaker firing activity of DA neurons[36] was enhanced in mNaChBac-expressing neurons and reduced
172 in Kir2.1 expressing neurons (Fig S4). Analysis by dSTORM of DAT distribution in mNaChBac expressing
173 neurons showed decreased clustering, while for Kir2.1 expressing neurons we saw a trend towards an
174 increased fraction of large clusters and a significant increase in localizations within large dense clusters
175 (Fig. 4A-D). Thus, DAT nanodomain localization is in cultured DA neurons regulated by persistent changes
176 in excitability or firing activity with increased activity leading to dispersal of DAT from nanodomains and
177 decreased activity leading to increased nanodomains localization.
178
179 **DAT nanodomain localization is regulated by Ca^{2+}.** Because of the effect of neuronal excitability, we
180 decided to investigate putative involvement of Ca^{2+} influx via voltage-gated Ca^{2+} channels (VGCC) in

181 NMDA-induced DAT declustering. Note that both P/Q type and N-type VGCCs should be present in DA
182 terminals [37]. DA neurons were stimulated with NMDA for 5 min with or without the N-type VGCC blocker
183 ω-conotoxin or the P/Q type VGCC blocker ω-agatoxin. While we observed no effect of ω-agatoxin, the
184 dispersing effect of NMDA on DAT clustering was essentially abolished by ω-conotoxin. Similarly, Voronoi
185 tessellation analysis showed that ω-conotoxin, but not ω-agatoxin, blocked the NMDA-induced shift away
186 from small, tessellated areas and thus blocked the dispersal of DAT nanodomains (Fig. 4E-J, Movies S1-2).
187 We next asked whether Ca^{2+} would be important *per se* by preincubating the neurons with the cell
188 permeable Ca^{2+}-chelator BAPTA-AM. Indeed, BAPTA-AM blunted the response to NMDA (Fig. 4K-L). Of
189 note, the pharmacological data fitted well with available single-cell mRNA sequencing data on DA neurons
190 supporting highest transcription of N-type VGCC in DA neurons (Fig. 4M). Taken together, NMDA-induced
191 dispersal of DAT nanodomains appears to occur via Ca^{2+}-dependent mechanism involving the activity of
192 N-type VGCCs.
193
194 **DAT nanodomain localization is regulated by the D2 autoreceptor.** D2-autoreceptors in DA neurons act
195 as negative feedback regulators decreasing neuronal excitability and firing activity by promoting opening
196 of inhibitory G-protein-activated inwardly rectifying potassium channels[38]. We surmised that D2-
197 autoreceptor activity might regulate localization of DAT to nanodomains and tested this by determining
198 the effect of the D2 receptor antagonist haloperidol and the D2 receptor agonist quinpirole. Interestingly,
199 incubation with 10 nM haloperidol for 5 min resulted in dispersal of DAT nanodomains with a reduced
200 fraction of clusters >75 m, fewer localizations in dense clusters and a reduced fraction of smaller Voronoi
201 tessellated areas (Fig. 5A-F, Movies S1, S3). This effect is likely the result of haloperidol blocking the effect
202 on the D2-autoreceptors of DA released in the culture as a consequence of DA neuronal pacemaker
203 activity as previously demonstrated for this culture of DA neurons[36]. Also, co-incubation with an excess of
204 quinpirole blocked the effect of haloperidol (Fig. 5A-F). Moreover, the effect of haloperidol was

205 accompanied by an increase in cytoplasmic free Ca^{2+} consistent with D2-autoreceptor activity suppressing
206 neuronal firing (Supplementary Fig. 5). This prompted us to test if the effect of haloperidol, like the effect
207 of NMDA, was dependent on Ca^{2+}- influx via N-type VGCCs. This appeared to be the case as ω-conotoxin,
208 but not ω-agatoxin, eliminated the effect of haloperidol (Fig. 5A-F). Summarized, our data support that
209 D2-autoreceptors are preoccupied with DA in the neuronal culture and that the activity of these receptors
210 can regulate DAT nanodomain localization via a Ca^{2+}-dependent mechanism.
211
212 **Single particle tracking supports nanodomain dispersal in response to neuronal activity.** To obtain a
213 better understanding of the dynamics underlying DAT nanodomain localization, we employed SPT-
214 dSTORM [20] to assess if dispersal of DAT from nanodomains is accompanied by increased lateral mobility
215 of DAT in the membrane. To allow visualization in live cells, we labeled DAT in DA neurons with a Janelia
216 Fluor®549-conjugated cocaine analogue, DG3-80, suited for live dSTORM[21] (Fig. 5G, H). Individual DAT
217 tracks were captured with lengths up to 1.6 sec (100 frames, 16 msec frame rate) with the majority being
218 10-20 frames (Fig. 5I, J). Separating tracks into those reflecting confined movements and those reflecting
219 freely moving particles showed that ~90% of the tracks described freely moving particles (Fig. 5K, L). Note
220 that this distribution (with most of the labeled molecules being freely moving) likely reflects preferential
221 binding of DG3-80 to unclustered DAT in the outward-facing conformation (Fig. 2). The mean jump
222 distance (i.e. the distance an individual molecule/particle has traveled between each image) was ~110
223 nm for all the recorded tracks and ~50 nm for static tracks only (Fig. 5M, N). Interestingly, a jump distance
224 of ~110 nm is so fast that a transporter molecule might move 7-14 µm during a transport cycle estimated
225 to last 1-2 sec[39]. Among the freely moving particles, there were even some that moved very fast with
226 mean jump distance of 200-350 nm (Fig. 5M-O). Both NMDA receptor activation and blockade of the D2-
227 autoreceptors with either haloperidol or the neutral antagonist UH-232 increased the population of DAT
228 molecules with mean jump distances >200 nm, indicative of a possible link between dispersal of DAT

229 nanodomains and increased lateral mobility. Note that the similar effect of UH-232 and haloperidol
230 strongly suggest that their effect reflects blockade of D2-autoreceptors activated by DA, which is released
231 because of DA neuronal pacemaker activity, and not inhibition of constitutive receptor activity[40].
232
233 **DAT nanodomains overlap with PIP2 nanodomains.** A key question is how the nanoscale distribution of
234 DAT relates to other molecular components of DA terminals. We first turned to the plasma membrane
235 phospholipid, PIP2, which can bind DAT and in doing so modulate DAT activity[41]. Dual-color dSTORM on
236 PIP2 and DAT in DA neurons showed as expected[42], a distribution of the PIP2 signal into nanodomains
237 (Fig. 6). Strikingly, these nanodomains showed a remarkable overlap with DAT nanodomains with the
238 Voronoi tessellation distributions revealing a large fraction of PIP2 localizations associated with dense
239 DAT localizations (Fig. 6A, B, F). As also seen for DAT domains, treatment with both NMDA and haloperidol
240 reduced PIP2 localizations in large dense clusters while haloperidol also reduced cluster size. Importantly,
241 all these changes were blocked by AP5 or quinpirole, respectively (Fig. 6B-D). The NMDA and haloperidol-
242 induced changes were reflected in the Voronoi tessellation distributions as well by showing dispersal of
243 the PIP2 nanodomains and reduced PIP2 association to nanoclustered DAT (Fig. 6E, F).
244
245 **The D2R is also shows nanodomain distribution.** We next analyzed the D2-autoreceptors that are found
246 both in the somatodendritic compartment of DA neurons and in DA terminals. Due to known challenges
247 with DA receptor antibodies, we first verified that our antibody was specific for the receptor in transfected
248 HEK293 cells (Supplementary Fig. 5). Subsequent dual-color dSTORM experiments on cultured DA
249 neurons revealed a clustered distribution of the D2-autoreceptors with nanodomains of a similar size as
250 those found for DAT (Fig. 7A, B). Furthermore, like our findings for DAT and PIP2, NMDA and haloperidol
251 promoted dispersal of the receptor domains (Fig. 7B-E). Relatively few of the nanodomains, however,
252 overlapped with the DAT domains as apparent from the Voronoi tessellation distributions (Fig. 7A, B, F),

253 and as for D2-autoreceptor association to DAT, we only observed marginal changes upon NMDA and
254 haloperidol treatment (Fig. 7F).

255 The findings prompted us to further assess the specificity of the pharmacological manipulations by
256 imaging additional key membrane components in DA terminals including clathrin[43] and the single
257 transmembrane SNARE protein syntaxin1 (STX-1). Imaging of clathrin revealed a nanoclustered
258 distribution, possibly corresponding to clathrin-coated pits[44], that showed little co-localization with DAT
259 and, importantly, essentially no change in distribution in response to NMDA (Supplementary Fig. 6). We
260 also recapitulated nanodomain distribution of STX-1 that is known to exist in such domains in presynaptic
261 terminals [45] as well as the protein has been proposed to bind DAT[46]. However, the STX-1 domains showed
262 little overlap with DAT and responded differently to NMDA with a decreased fraction of large clusters and
263 an increased fraction of localizations in dense clusters (Supplementary Fig. 6). Note, however, that NMDA
264 slightly increased localization of STX1 to unclustered DAT (i.e. the larger tessellated areas) according to
265 the Voronoi tesselated distributions (FIgure S6). In summary, several plasma membrane components of
266 DA terminals show a nanoclustered distribution that, however, appears to be differentially regulated.
267

268 **Discussion**

269 DA neurons have remarkable axonal arbors with numerous presynaptic terminals or varicosities that serve
270 as the principal architectural units responsible for release and reuptake of DA. Still, we have a surprisingly
271 poor understanding of the molecular organization of these varicosities, and what regulatory processes
272 that take place within these compartments less than ~1 µm in size. Indeed, most of these varicosities are
273 non-synaptic release sites and it remains unclear whether this results in less stringent requirement of the
274 spatial organization of the molecular machinery as compared to e.g. glutamatergic synapses[1-3]. Here, we
275 utilize several super-resolution techniques to provide detailed, quantitative insight into how a key
276 membrane protein, DAT, is subject to nanoscale regulation within these varicosities. This regulation
277 involves Ca^{2+}-dependent movements of DAT in and out of PIP2-enriched nanodomains in the plasma
278 membrane, which are governed by NMDA receptor and D2-autoreceptor activity and likely involves shift
279 of DAT between outward and inward-facing conformations.

280 To firmly substantiate that DAT is distributed into nanodomains in the plasma membrane of DA
281 neurons, we applied a range of different super-resolution microscopy techniques to both cultured
282 neurons and striatal slices. A varied label density cluster analysis[28] supported that our dSTORM procedure
283 reports true nanodomains, which was further confirmed by ExM, excluding potential artifacts from
284 multiple countings of the same fluorophore. A rough estimate of the number of DAT molecules suggested
285 the presence of 50-100 DAT molecules within each domain, which is in the same range estimated for
286 AMPA receptor domains in the postsynapse (~25 molecules)[47]. Importantly, by using the novel fluorescent
287 cocaine analogue DG3-63 and the disease-associated DAT mutant D421N, we were able to obtain
288 evidence that DAT displays a conformational bias depending on whether it is present in a nanodomain or
289 not. Based on these data, it is appealing to envision that a distribution of DAT between a nanoclustered,
290 inward-facing population of transporter molecules and an unclustered, “free” outward-facing population
291 of DAT molecules represents a means by which DAT activity can be regulated on a very fast time scale. A

292 possible question is whether this dynamic localization of DAT to nanodomains involves changes in DAT
293 oligomerization; however, we find this unlikely considering recent data supporting the existence in the
294 plasma membrane of DA dimers that are highly stable even over the course of minutes[48].

295 Of major importance, we validated in striatal slices the dispersing effect of NMDA on DAT
296 nanodomains by employing a novel Voronoi tessellation-based collection algorithm. In addition to
297 support that our findings in cultured DA neurons can be translated to intact tissue, the algorithm offers
298 possibilities for future detailed, quantitative analyses of protein distribution in neuronal terminals in
299 intact brain tissue. Another important observation was that both acute excitatory input, i.e. activation of
300 NMDA receptors, and sustained alterations of neuronal excitability, as evidenced by expression of either
301 mNaChBac or Kir2.1[34,35] in DA neurons, affect the nanoscale distribution of DAT in presynaptic varicosities.
302 We also observed a marked role of presynaptic D2R activity, further suggesting that the nanoscopic
303 distribution of a membrane protein, such as DAT, is continuously adapted by several mechanisms to the
304 immediate activity level of the neurons in which it is expressed. It may be considered that the effects of
305 the pharmacological manipulations on DAT clustering are quantitatively modest. However, the effects are
306 highly significant, as well as it should be considered that the numerous varicosities included in each
307 quantification may be very heterogenous and possibly differentially sensitive to treatments. Such
308 heterogeneity is directly supported by the finding that only a subset of DA terminals appeared active at
309 any given time[49]. Future efforts should further clarify this interesting issue.

310 Our data revealed a striking co-localization of DAT and PIP2 nanodomains, as well as a dispersing
311 effect of NMDA and haloperidol treatment on both types of domains. We also found that the effect of
312 haloperidol and NMDA on DAT nanodomains not only required opening of VGCCs but also was contingent
313 on the presence Ca^{2+}. Interestingly, an increase in cytosolic Ca^{2+} was previously shown to release
314 membrane protein sequestered PIP2, which might indicate a possible PIP2-dependent Ca^{2+}-regulation of
315 DAT nanodomain localization[50]. Indeed, the anionic lipid is known to form nanodomains that have been

316 suggested to be important for membrane protein nanoclustering, including STX-1[42]. Also, PIP2 is known
317 to regulate many cellular processes including ion channel and transporter function[51,52]. For DAT, it was
318 suggested that PIP2 binds to the DAT N-terminus and induces a structural change that encourages
319 phosphorylation and a reverse transport mode of DAT critical for amphetamine-induced DA efflux[41,51].
320 This is interesting in relation to our data that support an inward-facing configuration of nanodomain
321 localized DAT and thereby presumably a more efflux prone transporter[53]. Of note, our previous study
322 suggested a dependency on cholesterol for DAT nanodomain distribution[13]. Furthermore, previous data
323 have indicated that cholesterol binds to DAT and regulates its function by promoting an outward-facing
324 conformation[54]. A conceivable explanation is that cholesterol serves to compartmentalize the membrane
325 to enable a nanoclustered co-distribution of DAT and PIP2[55], and accordingly that cholesterol rather
326 interacts with unclustered, outward-facing DAT. It is even possible that rapid movements of DAT in and
327 out of nanodomains parallels the transport cycle shifting the transporter back and forth from an outward-
328 facing, substrate binding, conformation and unclustered distribution to an inward-facing, substrate
329 releasing (or efflux prone), conformation and clustered distribution. Indeed, our single particle tracking
330 data (Spt-STORM) show that the mean jump distance for a given particle is r~110 nm in a 16 ms time fram
331 (Fig. 5M), suggesting that a single DAT molecule moves 7-14 µm during a single transport cycle of 1-2
332 sec[39]. Thus, the movements in the membrane are fast enough for DAT molecules to move in and out of
333 nanodomains during a single transport cycle. Fast movements of DAT have also been supported with
334 classical single particle tracking techniques[21] although use of large quantum dots for labeling suggested
335 somewhat slower diffusion speeds[56].

336 Previous data have indicated that stimulation of D2-autoreceptors of both the D2 and D3 subtype
337 enhance DAT activity[38,57-59]. Here we provide evidence that in the DA neuronal cultures the D2-
338 autoreceptor is preoccupied with DA and that this promotes DAT nanoclustering, consistent with such an
339 enhancement; that is, if D2-autoreceptor activation causes an increase in DAT activity, this would

340 expectably lead to a shift of the DAT conformational equilibrium towards a more inward-facing
341 conformation and, hence, a likely shift towards a higher degree of nanodomain localization. However, our
342 data may challenge that the regulation of DAT by D2-autoreceptors involves a direct interaction as
343 previously suggested[57,58]. Although the D2-autoreceptor, like DAT, according to our dSTORM analyses, are
344 distributed into nanodomains, we observed only modest co-localization between the two proteins in the
345 DA terminals. The nanodomains responded, nonetheless, like DAT to NMDA and haloperidol, suggesting
346 that excitatory input promotes nanodomain dispersal, while D2 autoreceptor activation promotes
347 nanoclustering. We speculate that this increased clustering upon activation reflects assembly of the
348 receptor with intracellular signaling complexes and/or dynamics relating to desensitization and/or
349 internalization.

350 DAT nanodomains showed rather little co-localization with nanodomains of STX-1 and clathrin that
351 importantly also responded differently to NMDA. These differential effects support that the changes we
352 see for DAT, the D2-autoreceptor and PIP2 most likely reflect true molecular redistributions and unlikely
353 are the result of non-specific changes. The decrease in STX-1 nanocluster size and increased localization
354 within dense clusters in response to NMDA is consistent with other studies indicating that breakup of STX-
355 1 nanodomains, correlating with vesicle release, takes place, while at the same time more STX-1 is being
356 brought to the sites of release[45,60]. Of interest, the Voronoi tesselated distributions showed that NMDA
357 slightly increased localization of STX1 to unclustered DAT (i.e. the larger tessellated areas). This suggests
358 that the previously described direct interaction between DAT and STX-1, which have been proposed to
359 be important for amphetamine-induced efflux[46], may take place between the unclustered fractions of the
360 two proteins.

361 Summarized, by application of single-molecule sensitive super-resolution imaging we show
362 compelling evidence that the molecular machinery supporting volume transmission mediated by a
363 neuromodulator like DA is subject to spatial and temporal nanoscale regulation with putative major

364 impact on synaptic function. The conclusion is substantiated by detailed studies of DAT that according to
365 our results is subject to remarkable nanoscale regulatory processes governed by excitatory input,
366 membrane potential, Ca^{2+} and activity of the presynaptic D2 receptor. Taken together, the present results
367 not only constitute a new framework for further deciphering the nanoscale architecture of presynaptic
368 release sites and the underlying functional implications for the DA system but also add to the growing
369 acknowledgment of nanoscopic regulation as a still poorly explored area of fundamental importance for
370 neuronal signaling.
371
372

373 **Methods**

374 **Molecular biology, virus generation and virus transduction.** The cDNA encoding human DAT (synthetic
375 gene kindly provided by Dr. Jonathan Javitch, Columbia University, NY, USA[61] was inserted into pmEOS2-
376 C1 (RRID: Addgene#54510) to generate pmEOS2-hDAT C1 encoding hDAT with mEOS2 fused to the N-
377 terminus. Plasmids encoding WT hDAT and D421N hDAT (pRC/CMV hDAT and pRC/CMV hDAT D421N)
378 were generated as described[32]). The cDNA encoding the short transcriptional variant of human DA D2
379 receptor with an N-terminal FLAG tag (SF-D2R-S) was inserted into mammalian expression vector pcDNA
380 3.1(+) (Invitrogen)[62]. The Cre-dependent construct, pAAV-CAG-Flex-NES-jRGECO1a-WPREpA, was
381 obtained from Addgene (RRID: Addgene #100854). The plasmids, pAAV-hSyn-DIO-mNaChBac-T2A-
382 mKate2-WPREpA and pAAV-hSyn-DIO-Kir2.1-T2A-mKate2-WPREpA, were SLIC cloned[63] from pAAV-EF1α-
383 F-FLEX-mNaChBac-T2A-tdTomato (RRID: Addgene #60658) and pAAV-EF1α-F-FLEX-Kir2.1-T2A-tdTomato
384 (RRID: Addgene #60661), respectively, into a Cre-dependent AAV backbone plasmid with a mKate2
385 fluorophore instead of tdTomato. This was done to make them sufficiently short so that packaging into
386 an AAV capsid would be feasible (ITR to ITR length<4700 kbp). The pAAV-pTH-iCre-WPREpA construct was
387 created and cloned in-house and contains a truncated 488bp rat TH promoter encoding Cre recombinase.
388 In-house generated AAVs were produced using a FuGene6 (Promega) mediated triple plasmid co-
389 transfection method in HEK293t cells. Three days after transfection, cells were harvested and virus
390 purified using an adapted Iodixanol gradient purification protocol [64]. Genomic AAV titer was determined
391 by a PicoGreen-based method as described elsewhere [65] AAV2-retro-pTH-iCre mediated expression of
392 Cre-dependent jRGECO1 was verified by fluorescence microscopy and no differences were observed
393 across the different titers used. For transduction, the appropriate virus was applied to primary culture DA
394 neurons at an approximate concentration of 2*10E9 vg/mL at 1 to 3 days after preparation of the
395 neuronal cultures.

396 **Primary cultures of DA neurons with cortical glia cells.** Cultured glial cells were obtained from cortex and
397 cultured DA neurons were obtained from the midbrain of P1-P3 Wistar rats (Charles River, Germany).
398 Gender was mixed as the cultures were generated from a mixed sex populations of rat pups. For
399 preparation of cultured glial cells, brains were removed from euthanized P1-P3 pups and placed in
400 phosphate-buffered saline (PBS) on ice. The cortex of each brain was isolated and cut into millimeter sized
401 sections and collected in cold dissection medium (Hanks' Balanced Salt Solution with added Sodium
402 Pyruvate (1 mM), Penicillin-Streptomycin (Sigma P0781, 200 U/L), 10 mM HEPES, and 0.54% glucose)).
403 After collecting all, the dissection medium was replaced with glia cell medium (DMEM with HEPES "1965",
404 FBS (10%), Penicillin-Streptomycin (60 U/L)). The tissue was mechanically titrated through pipetting up
405 and down using a flame-polished Pasteur pipette followed by straining through a 70 µm cell trainer and
406 centrifugation for 10 min at 200-300 x g. The pellet was resuspended in 10 mL glia medium and strained
407 again before a second centrifugation for 10 min at 200-300 g and removal of the supernatant. The pellet
408 was resuspended and seeded into large T175 flasks at approximately 1.5 brains per flask with added glial
409 medium to a total of 20 mL. Glia cells were grown in an incubator at 37◦ C with 5% CO_2 until they were
410 70% confluent. The cells were either frozen in heat-inactivated serum containing 10% DMSO for later use
411 or applied to ethanol-cleaned and poly-D-lysine-coated coverslips and incubated for 1 week prior to DA
412 neuron addition. On the day before DA neuron addition, the glial cells were changed to DA neuron
413 medium (Neurobasal A with heat-inactivated FBS (1/100), GlutaMAX (1/100) B-27 (1/50), ascorbic acid
414 (200 µM), Penicillin-Streptomycin (60 U/L), kynurenic acid (0.5 mM)). Midbrain DA neurons were
415 generated using a protocol modified from[36]. Brains from rat pups (P1-P3) were isolated and placed in PBS
416 on ice. Midbrain sections were retrieved from each brain as the brains were cut while in dissection buffer.
417 The midbrain sections were transferred to papain solution (cysteine (1 mM), DNase (0.1 mg/mL), papain
418 (20 units/mL), NaCl (116 mM), KCl (5.4 mM), $CaCl_2$ (1.9 mM), NaHCO3 (26 mM), $NaH_2PO_4H_2O$ (2 mM),
419 $MgSO_4$ (1 mM), EDTA (0.5 mM), Glucose (25 mM), kynurenic acid (0.5 mM) in water) for 30 min at 37◦C.

420 The solution was replaced with prewarmed DA medium and samples were mechanically titrated with
421 flame polished Pasteur pipettes and the resulting suspension centrifuged at 200-300 x g for 10 min. The
422 pellet was resuspended in DA neuron medium and applied to each culture. Glia-derived neurotrophic
423 factor (GDNF) (100ng/mL of culture solution volume) was applied immediately after seeding of the
424 neurons. Cultures were incubated for 2 to 3 weeks prior to use. All procedures were performed according
425 to institutional guidelines at the Faculty of Health Sciences, University of Copenhagen.
426
427 **Transfection of DA neurons.** Primary cultures of DA neurons were transfected using magnetotransfection
428 at ~14 DIV[66]. NeuroMag reagent (OZ biosciences) (8 µL) was mixed with plasmid (4 µg) and DA neuron
429 medium (200 µL). The mixture was incubated for 20 min at RT before it was added to cultures grown in
430 6-well plates. The culture was positioned on top of a magnetic plate for 15 min after which the culture
431 before it was moved back to the cell incubator and used for immunostaining 24-48 hours later.
432
433 **Immunostaining of primary cultures of DA neurons for dSTORM and PALM.** The cell samples were fixed
434 in paraformaldehyde (3%) and washed three times in glycine (20 mM) and NH_4Cl (50 mM) in PBS.
435 Subsequently, the cells were washed in blocking buffer (5% Donkey serum, 1% BSA in PBS), and incubated
436 in blocking permeabilization buffer (blocking buffer with saponin (0.2%)). Primary antibody was applied
437 in blocking buffer for 60 min, followed by 3–5 min incubation in blocking buffer. Secondary antibody was
438 applied in blocking buffer for 45 min, and the sample was incubated 2x for 5 min in blocking buffer.
439 Samples were washed in PBS twice and post-fixated in paraformaldehyde (3%) for 15 min. Samples were
440 washed twice in glycine (20 mM) and NH_4Cl (50 mM) in PBS and stored in PBS at 4°C until imaging.
441

442 **Mouse brain slices.** Mouse brain slices were obtained from male C57BL/6 mice 12-16 weeks old. The
443 slices were prepared as described below. All procedures were performed according to institutional
444 guidelines at the Faculty of Health Sciences, University of Copenhagen.
445
446 **Preparation and immunostaining of mouse brain slices for dSTORM.** Mice were anesthetized with
447 isoflurane and perfused first with PBS followed by 4% paraformaldehyde (PFA) injected directly into the
448 heart. Brains were then placed in 4% PFA for 24 hours, followed by sucrose (30%) for 24 to 48 hours.
449 Subsequently, brains were snap-frozen on powdered dry ice and stored at -80°C. The brains were sliced
450 using a cryostat (Leica CM3050 S) to obtain 10 µm striatal coronal sections and each slice was immediately
451 fused to a 3-aminopropyltriethoxysilane coated coverslip and let dry at room temperature before being
452 stored in antifreeze (50% glycerol 50% PBS) at -20 ◦C. For immunostaining, brain sections were first rinsed
453 3x in PBS and subsequently washed 2x with 15 min incubation in glycine (20 mM) and NH_4Cl (50 mM) in
454 PBS. This was followed by 30 min wash in 10 mM trisodium citrate, pH 6.0, preheated to 80◦ C, 4x wash
455 in PBS and then blocking/permeabilization for 30 min in PBS with 5% donkey serum, 1% BSA and 0.3 %
456 Triton X-100. Primary antibody was applied overnight in blocking/permeabilization buffer followed by
457 washing in 5/5/90 min increments and application of secondary antibody overnight in
458 blocking/permeabilization buffer. Sections were again washed in 5/5/90 minute increments in
459 blocking/permeabilization buffer and then with 5/5 min increments with PBS. The sections were post-
460 fixated in paraformaldehyde (3%) and washed twice for 15 min in glycine (20 mM) and NH_4Cl (50 mM) in
461 PBS. Samples were lastly washed twice in PBS and stored in PBS at 4 ◦C until imaging.
462
463
464 **Antibodies and labeling.** Secondary antibodies (donkey anti-rat, Jackson 712-005-153, RRID:AB_2340631;
465 donkey anti-mouse, Jackson 715-005-151, RRID:AB_2340759); or donkey anti-rabbit, Jackson 711-005-

466 152, RRID:AB_2340585) were labeled with either NHS-ester conjugated Alexa647 or CF™568 (Biotium,
467 Freemont, CA) and then isolated through Zeba™ Spin Desalting Columns, 40K MWCO (ThermoFisher
468 87767). This was completed by first washing the column 3x with 300 µL of 100 mM $NaHCO_3$ in PBS.
469 Following the washes, 50 µg of antibody in 100 µL of PBS was added and spun at 1500 x g for 2 mins. The
470 flow-through was collected and combined with a 5-fold molar excess of NHS ester fluorophore. This
471 solution was incubated in the dark at RT, shaking, for 2.5 hours. A new spin column was then washed 3
472 times with NaN--3 (0.02%) in PBS. The antibody sample with the dye was then added to the column and
473 centrifuged for 2 min at 1500 x g. The protein concentration and label concentration of the final product
474 were measured on a NanoDrop 2000 Spectrophotometer (ThermoFisher). Labeled antibodies had
475 between 1 and 2 fluorophores attached.
476 We used the following antibodies and fluorophores for our imaging analysis:

Antibody Target	Product Number	Experiment	Dilution	Secondary antibody	Fluorophore
DAT	Millipore MAB369 RRID:AB_2190413	Primary culture dSTORM	1/200	5 µg/mL Donkey anti-Rat	Alexa647
DAT	Millipore MAB369 RRID:AB_2190413	IHC dSTORM	1/200	10 µg/mL Donkey anti-Rat	Alexa647
DAT	Millipore MAB369 RRID:AB_2190413	Expansion (ExM)	1/200	5 µg/mL Donkey anti-Rat	Atto 643N
TH	Millipore MAB318 RRID:AB_2201528	PALM/dSTORM	1/500	5 µg/mL Donkey anti-Mouse	Alexa647
STX-1	Synaptic Systems 110 011 RRID:AB_887844	Primary culture dSTORM	1/500	5 µg/mL Donkey anti-Mouse	CF568
Clathrin light chain	Synaptic Systems 113 011 RRID:AB_887706	Primary culture dSTORM	1/500	5 µg/mL Donkey anti-Mouse	CF568
PIP2	Abcam ab11039 RRID:AB_442848	Primary culture dSTORM	1/500	5 µg/mL Donkey anti-mouse	CF568
D2R	Synaptic Systems 376 203 RRID:AB_2636918	Primary culture dSTORM	1/500	5 µg/mL Donkey anti-rabbit	CF568
mKate2	Evrogen AB233 RRID:AB_2571743	Primary culture dSTORM	1/500	5 µg/mL Donkey anti-rabbit	CF568

477
478

479 **Expansion Microscopy (ExM).** For ExM, perfused brains were acquired by injecting first PBS and then 4%
480 PFA into the heart of anesthetized mice. Brains were postfixated in 4% PFA for 24 hours and immersed in
481 sucrose solution (30%) for 24 to 48 hours. Coronal brain slices (40 µm) were obtained with a cryostat. The
482 brain slices were stored, free floating, in antifreeze (50% glycerol 50% PBS) at -20◦C until use. Brain slices
483 were washed with PBS three times, and then permeabilized in blocking buffer (5% donkey serum, 1%
484 bovine serum albumin, 0.1% Triton X-100, in PBS). Brain slices were incubated overnight with primary
485 antibody in blocking buffer (5% donkey serum, 1% bovine serum albumin, 0.1% Triton X-100, in PBS, pH
486 7.4). Slices were washed 4x in blocking buffer with 30 min increments and incubated overnight with
487 secondary antibody in blocking buffer at 4◦C. Slices were again washed 4x in blocking buffer with 30 min
488 increments. Anchoring treatment was performed with Acryloyl-X-SE (0.1 mg/mL) in PBS at room
489 temperature overnight[18]. Gel solution was made by mixing N,N-dimethylacrylamide (1.335 g) and sodium
490 acrylate (0.32g) in 2.85 g of water. Oxygen was purged with nitrogen gas for 40 min. 2.7 mL of the gelling
491 solution were mixed with 0.3 mL 0.036 g/mL solution of potassium persulfate ($K_2S_2O_8$) solution and purged
492 of oxygen with nitrogen gas for 15 min on ice. Brain slices were transferred to the extra gelling solution
493 and placed flat on poly-D-Lysine coated glass slides. Excess gelling solution was removed, and glass
494 coverslips were placed on the edges of each slice to limit gel dispersion. All work from this point was
495 done in a cold room (4◦C). Aliquots of 500 µL of polymerization solution were combined with 2 µL of
496 TEMED was added and the solution vortexed before applying 80 µL to brain slices. A layer of parafilm
497 covered coverslip was placed overtop of the gel to fully surround the gel. The sample was kept in the cold
498 room for 15 min before being brought back out to room temperature. The container with the gels was
499 filled with nitrogen and wet paper to keep humidity and made airtight. Following gelation, samples were
500 carefully cut out from the chamber in a sim-card shape to ensure orientation. Gels were measured in size
501 and placed in digestion buffer overnight at room temperature (50mM TRIS, 800 mM guanidine HCl, 2 mM
502 CaCl2, 0.5% Triton X-100, proteinase K 8U/mL, pH 8.0). The gels were placed into individual dishes and

503 dialyzed with water many times over a day until they no longer expanded. Imaging was performed the
504 next day on a spinning disk confocal microscope (FEI CorrSight utilizing a C-Apochromat 63x/1.20 W Corr
505 M27 objective). Samples were places dry on poly-D-Lysine coated chambers and water was added to the
506 top of the gel just enough so the gel was hydrated but not so it would move around.
507
508 **dSTORM.** For dSTORM we used a buffer containing β-mercaptoehtanol and an enzymatic oxygen
509 scavenger system (10% (w/V) glucose, 1% (V/V) beta-mercaptoethanol, 2 mM cyclooctatetraene, 50 mM
510 Tris-HCl (pH 8), 10 mM NaCl, 34 µg mL^{-1} catalase, 28 µg mL^{-1} glucose oxidase). The imaging was performed
511 with an ECLIPSE Ti-E epifluoresence/TIRF microscope (NIKON, Japan) equipped with 405 nm, 488 nm 561,
512 and 647 nm lasers (Coherent, California, USA). All lasers are individually shuttered and collected in a single
513 fiber to the sample through a 1.49 NA, 100x, apochromat TIRF oil objective (NIKON). Single color imaging
514 was done with a dichroic mirror (z405/488/561/647 rpc) and the emitted light was filtered by a 710/80
515 nm bandpass filter. For dual-color dSTORM, we used a dichroic mirror with the range 350–412, 485–490,
516 558–564, and 637–660 nm (97,335 QUAD C-NSTORM C156921). The excitation light was filtered at the
517 wavelengths: 401 ± 24 nm, 488 ± 15 nm, 561 ±15 nm, 647 ± 24 nm. The emitted light was filtered at the
518 wavelengths: 425-475, 505-545, 578-625, and 664-787 nm, and secondly by an extra filter to decrease
519 noise (561 nm Longpass, Edge Basic, F76-561, AHF). A motorized piezo stage controlled by a near-infrared
520 light-adjusted perfect focus system (NIKON) is applied to the system to reduce any sample drift over time
521 in the z-direction. Single-color dSTORM images were constructed from 30,000 frames taken at a 16 ms
522 frame rate. Dual-color dSTORM images were constructed from 20,000 frames for each color taken at a 16
523 ms frame rate with each color alternating by frame. Photons were collected with an iXon3 897 EM-CCD
524 camera camera (Andor, United Kingdom). Laser powers used were 2.3 kW cm −2 for 647 nm, 1.0 kW cm−2
525 for 488 nm and for 561 nm. The 405 nm laser was used to incrementally increase blinking behavior at
526 power <0.1 kW cm−2. For 3D-dSTORM, a cylindrical lens was placed before the camera to impart

527 astigmatism. To verify the multicolor alignment of our microscope, dSTORM images of 100 nm Tetraspek
528 beads were taken. Localizations were fit to widefield illuminated Tetraspec beads and processed as our
529 dSTORM data is processed (Supplementary Fig. 7).
530
531 **PALM.** For PALM imaging of mEos-DAT, we obtained 5,000 consecutive frames with a frame rate of 33 Hz
532 to construct one image. The 488 nm excitation laser was held constant, 0.4 kW cm^{-2}, during the capture
533 of the image while the 405 nm activation laser was gradually increased to <0.1 kW cm^{-2}.
534
535 **Localization fitting of dSTORM data.** 2D localizations were fit with ThunderSTORM using local maximum
536 detection with a threshold of 1.5 *std(Wave.F1) and estimator of an integrated gaussian PSF. Sigma was
537 1.6, fit radius was 3 pixels, and weighted least squares was the method to fit the estimated gaussian to
538 the PSF[67]. 3D localization fitting was performed with fit3Dcspline[44]. 3D calibrations were made on 100 nm
539 TetraSpeck beads attached to a coverslip by first placing 50 µL of MgCl2 (1M) on the coverslip and then
540 adding 500 L of water with 0.9 µL of TetraSpeck beads to the coverslip. Drift for all data was corrected
541 with redundant cross correlation through Matlab[68]. Localizations were filtered for uncertainty being less
542 than 25 nm and then merged for localizations that were detected within 15 nm and 3 frames.
543
544 **Data processing pipeline – dSTORM.** To perform necessary localization fitting on the 1349 dSTORM
545 images included in this study, an in-house data processing pipeline was developed to streamline
546 operations. Localizations were fit to the raw data with the aforementioned settings in ThunderSTORM
547 through a self-written ImageJ macro. Although ThunderSTORM can perform the remaining processing
548 steps, a custom python script (utilizing Matlab functions) was written to perform cross correlation,
549 merging and filtering so that redundant cross correlation could be employed. The images were then
550 blinded by labeling them with a random integer and saving the cypher elsewhere. Through a separate

551 custom Matlab script, varicosities were selected from each image though a freehand selection.
552 Varicosities were identified by the local swelling of their structure compared to the rest of the extension.
553 We next used DBSCAN (density based spatial clustering of applications with noise)[13,24] to identify clusters
554 by size or for determining localizations in dense clusters through the use of a python script employing the
555 DBSCAN method from the sklearn python library. Voronoi tessellation [25] was employed through Matlab.
556 The Voronoi based density association algorithm was also written in house and using Matlab.
557
558 **Varicosity identification in dSTORM DA neuron culture data.** Automatic varicosity identification could
559 not discern between extension and varicosity, so these were selected through a freehand ROI taken of
560 blinded files. Localization data for all images in a given dataset were blinded by being randomly assigned
561 a number that was stored on a cypher. ROIs were then gathered without the knowledge of the image
562 identity, with this information restored in the analysis of the ROIs.
563
564 **Varicosity identification in brain slice dSTORM data.** As this was a computationally intensive process,
565 each image was divided into 100 quadrants in a 10x10 grid. Within each quadrant, the localizations were
566 sub-sampled down to 1000 random localizations, and the Voronoi tessalation was obtained for that
567 section. Tesselated areas were filtered for having an area less than 15000 nm^2. Tesselated shapes that
568 were touching one another were merged together. Shapes were now filtered for possessing an area
569 greater than 300000 nm^2. These ROIS were buffered by 50 nm along each edge to smooth the ROI.
570
571 **Clustering analysis of dSTORM data.** Cluster size was identified by performing DBSCAN on each varicosity
572 for a radius of 15 nm and 5 localizations being the cluster qualifier. The convex hull was gathered for each
573 cluster to find its area, and the fraction of clusters with a diameter >75 nm was used for the cluster size
574 analysis. Cluster size distributions were not shown as clusters reaching the detection limit of this method

575 are not accurate and cause a false perception on the cluster size distribution. Localizations in dense
576 clusters were found by applying DBSCAN to each varicosity with a radius of 50 nm and 80 localizations
577 being the qualifier. Voronoi tessellation was applied to each varicosity and areas were filtered for sizes
578 between 5 nm2 and 1000 nm2. Probability density functions were created for these distributions.
579
580 **Density Association.** Density association was found by performing Voronoi tessellation on target A, and
581 finding all points in target B that were 25 nm from any point in target A. Each of these target B points that
582 possessed A association were mapped to the Voronoi tessellated area from target A they resided in. The
583 probability density functions for target A and the areas from target A that had an associated target B were
584 created. This procedure was applied to compare the dSTORM signal of DG3_63 to mEOS2-DAT, STX1 to
585 DAT, D2R to DAT, PIP2 to DAT, and clathrin to DAT.
586
587 **Quantification of DAT molecules in nanodomains.** Primary DA neurons were labeled and imaged for
588 dSTORM with the DAT MAB369 antibody at dilutions 1:200, 1:400, 1:800, 1:1600, 1:3200. Varicosities
589 were manually selected from blinded data files. Clusters of localizations potentially arising from single
590 localizations were identified in the varicosities found in the 1:3200 dilution data set through DBSCAN with
591 the parameters [ε = 30 nm, nps = 2]. A histogram was made comparing the number of localizations found
592 per cluster from this cluster analysis, and 3 localizations was determined to be the estimate for the
593 number of localizations arising from a single monoclonal antibody in this image set. Clusters were then
594 found in the remaining dataset through the same method defined to identify cluster size. A histogram
595 was made to show the number of localizations present within the clusters found with a diameter >75 nm.
596 The peak of this histogram was ~100 localizations, suggesting there are roughly 33 primary antibodies
597 labeling DAT within a given cluster/nanodomain of this size.
598

599 **Varied label density cluster verification.** Varicosities used for the counting experiment were subject to
600 the varied label density cluster verification test[28]. Sig for gaussians was set to 15 nm and the cut gauss at
601 x times sig was set to 2. The threshold selected was 2.
602
603 **Labeling and imaging primary cultures with DG3-63.** Live primary cultures were labeled with DG3-63 (20
604 nM) [21] for 10 min in the dark at room temperature and washed 3 times with aCSF (NaCl (120 mM), KCl (5
605 mM), $CaCl_2$ (2 mM), $MgCl_2$ (2 mM), 1 mM NaH_2PO_4, HEPES (25 mM), glucose (30 mM), pH 7.4). Samples
606 were fixed with paraformaldehyde (3%) for 15 min followed by 3 washes with glycine (20 mM) and NH_4Cl
607 (50 mM) in PBS. Samples were imaged in normal dSTORM buffer.
608
609 **Heterologous cell culture.** Cath.a-differentiated (CAD) cells[69] (ATCC CRL-11179 or Sigma-Aldrich
610 08100805) originated from mouse (B6/D2 F1 hybrid) catecholaminergic neuronal tumor. The cells were
611 maintained in a 1:1 mixture of DMEM 1965 and Ham's F-12 medium (Invitrogen), both supplemented
612 with 10% FBS and 0.01 mg/mL gentamicin. HEK293 cells (human embryonic kidney cells, ATCC CRL-1573)
613 were grown as described[32].
614
615 **Transfection of CAD cells and labeling with DG3-63.** CAD cells were transfected with pmEOS2-hDAT
616 encoding mEOS-DAT or with pRC/CMV-hDAT or pRC/CMV-hDAT D421N encoding WT DAT and the DAT
617 mutant D421N, respectively[32]. The CAD cells (~1 million cells) were seeded the day before transfection in
618 a 25 cm^2 flask and washed on the day of transfection before addition of 5 mL of medium. For the
619 transfection, 1 µg of DNA was added to 100 µL of optiMEM as well as 3 µL Lipofectamine (Invitrogen) to
620 a separate 100 µL of optiMEM. After 5 min, the two solutions were mixed and incubated for 30 min before
621 the total mixture was added to the cells. The next day the cells were harvested and seeded on poly-D-
622 Lysine coated coverslips (100,000 cells per coverslip). For DG3-63 labeling experiments, the media was

623 removed the next day from the mEOS-DAT expressing cells and 1 mL of aCSF was added (NaCl (120 mM),
624 KCl (5 mM), $CaCl_2$ (2 mM), $MgCl_2$ (2 mM), HEPES (25 mM), glucose (30 mM), pH 7.4) before incubation for
625 10 min with or without 100 µM unlabeled cocaine. Following this, the cells were labeled with 10 nM DG3-
626 63 [21] for 10 min in aCSF. Samples were washed 3 times with aCSF and then fixed for 15 min in
627 paraformaldehyde (3%) followed by 2x wash with glycine (20 mM) and NH_4Cl (50 mM) in PBS. Samples
628 were imaged in dSTORM buffer as described above. For dSTORM of hDAT WT and D421N, cells the cover
629 slips samples were stained in the same fashion as primary DA cultures.
630
631 **Pharmacological treatment of acute brain slices.** Mice were euthanized with isoflurane and the live
632 brains were removed. Coronal sections, 300 µm thick, were cut with a vibratome in cold aCSF (NaCl (119
633 mM), KCl (2.5 mM), NaH_2PO_4 (24 mM), Glucose (12.5 mM), $CaCl_2$ (2 mM), $MgCl_2$ (2 mM)) that was being
634 aerated with carbogen gas. Brain slices were transferred to aCSF and maintained for 1 hour at room
635 temperature under constant carbogenation. Slices were then transferred to either aCSF or aCSF with AP5
636 (100 µM), both at 37◦ C for 10 min. Slices from normal aCSF were moved to aCSF with or without NMDA
637 (20 µM). The NMDA containing aCSF had reduced magnesium (0.3 mM MgCl2) and added glycine (100
638 µM). The samples from AP5 were transferred to aCSF with AP5 (100 µM) and NMDA (20µM), reduced
639 magnesium (0.3 mM $MgCl_2$), and added glycine (100 µM). These incubated for 5 min, and then the slices
640 were transferred to paraformaldehyde (3%) overnight at 4◦ C. Slices were transferred to a 30% sucrose
641 solution for 2 days a 4◦C and then placed into plastic molds and covered with Tissue-Tek O.C.T. and stored
642 at -80◦C. Samples were sliced at 10 µm on the cryostat and stained for dSTORM.
643
644 **Pharmacological treatment of primary cultures.** In general, treatments were performed by replacing the
645 media at room temperature with aCSF (NaCl (120 mM), KCl (5 mM), $CaCl_2$ (2 mM), $MgCl_2$ (2 mM), 1 mM
646 NaH_2PO_4, HEPES (25 mM), glucose (30 mM), pH 7.4) followed by stimulation with indicated compounds.

647 For the NMDA or haloperidol experiments with testing of VGCC inhibitors, cells were treated for 10 min
648 with either control aCSF, AP5 (100 µM) or quinpirole (50 µM), ω-conotoxin (1 µM), ω-agatoxin (1 µM).
649 Samples were then treated for 5 min with these same concentrations as cotreatment with either NMDA
650 (20 µM) or haloperidol (10 nM). NMDA treatments were done in aCSF with added glycine (100 µM). All
651 experiments using NMDA were done with aCSF with reduced magnesium (0.3 mM $MgCl_2$) for all
652 conditions. For the BAPTA-AM experiment, the pretreatment with BAPTA-AM (25 µM) was for 30 min
653 prior to the 5-min NMDA (20 µM) treatment.
654
655 **SPT-dSTORM.** Live primary cultures were labeled with DG3-80 (20 nM) for 10 min and then washed 3
656 times with aCSF (NaCl (120 mM), KCl (5 mM), $CaCl_2$ (2 mM), $MgCl_2$ (2 mM – 0.3 mM for NMDA related
657 experiments), 1 mM NaH_2PO_4, HEPES (25 mM), glucose (30 mM), pH 7.4). A suitable location to image
658 was found while the sample was kept in aCSF, and then SPTdSTORM imaging was done in a modified
659 dSTORM buffer (560 µg/mL glucose oxidase, 34 µg/mL catalase, 1.4 µL/mL β-Mercaptoethanol in aCSF).
660 Pharmacological treatments were done 5 min before imaging with either 20 µM NMDA with 100 µM
661 glycine, 200 nM haloperidol, or 1 µM UH-232. AP5 (100 µM) was applied for 10 min prior to cotreatment
662 with NMDA. Imaging was performed at room temperature on the NIKON TiE Eclipse TIRF microscope
663 described under dSTORM. Light with a wavelength of 561 nm at 0.3 kW cm^{-2} was utilized to promote
664 blinking of the fluorophores. Images were collected with 16 ms frame rate. Localizations were fit using
665 ThunderStorm as described above. Single molecule trajectories were found using the program swift [70].
666 Parameter used beyond the default were: ”expdisplacement” : 300,”expnoiserate”:
667 10,”maxblinkingduration” : 2,”pblink” : 0.5,”preappear” : 0.5,”pswitch” : 0.001,”precision”:
668 30,”pruningbase” : 2,”pruningrate” : 0.2,”randomseed” : 42,”wdiffusion” : 2,”wdirected” : 1,”wfield” :
669 0,”wimmobile” : 1.
670

671 **Electrophysiology recordings of DA neurons.** DA neuronal cultures were transduced after 3 DIV (days in
672 vitro) with pAAV-pTH-iCre-WPREpA plus either pAAV-hSyn-DIO-mNaChBac-T2A-mKate2-WPREpA or
673 pAAV-hSyn-DIO-Kir2.1-T2A-mKate2-WPREpA. Electrophysiological recording by the whole-cell patch
674 clamp technique were done 2-3 weeks after transduction. The DA neurons expressing either mNaChBac
675 or Kir2.1 were identified based on mKate2 fluorescence using an upright microscope (Olympus BX51WI).
676 For the recordings, the cultures were submerged in circulating, heated, and oxygenated aCSF (in mM;
677 NaCl 125, KCl 2.5, $NaHCO_3$ 26, $CaCl_2$ 2, $MgCl_2$ 1, NaH_2PO_4 1.25, Glucose 25; 2 ml/min, 35°C). The aCSF was
678 supplemented with NBQX (20 µM). The patch glass electrode was filled with (in mM) K-gluconate 122,
679 Na_2-ATP 5, $MgCl_2$ 2.5, $CaCl_2$ 0.0003, Mg-Gluconate 5.6, K-Hepes 5, H-Hepes 5, and EGTA 1, and had tip
680 resistance of 4-6 MΩ. After break-in, the cells were held at 0 pA in current clamp mode to measure the
681 pacemaker activity. Recordings were acquired with a Multiclamp 700B amplifier and 1440A Digitizer.
682

683 **Calcium Imaging of DA neurons.** Primary DA neurons were prepared as described above but instead of
684 culturing the neurons on glass coverslips, they were cultured on MatTek 35 mm 14 mm glass microwell
685 (no 1.5) glass bottom dishes (MatTek). To enable measurement of Ca^{2+}-fluctuations specifically in DA
686 neurons, the neurons were transduced with an AAV encoding double-floxed jRGECO1a (AAV-CAG-Flex-
687 NES-jRGECO1a-WPREpA) together with an AAV encoding Cre recombinase under control of a truncated
688 TH promoter (AAV2-retro-pTH-iCre-WPREpA). The cell medium was changed to aCSF (NaCl (120 mM), KCl
689 (5 mM), CaCl2 (2 mM), $MgCl_2$ (2 mM), 1 mM NaH_2PO_4, HEPES (25 mM), glucose (30 mM), pH 7.4)
690 immediately prior to imaging. Imaging took place at room temperature on the NIKON TiE Eclipse TIRF
691 microscope described above. Once a suitable neuron was located, the sample was imaged with 561 nm
692 light (10 W cm^{-2}). Videos were collected with a 16 ms frame rate. Haloperidol was added mid-video so
693 that the sample had a total concentration of 10 nM Haloperidol. Data was collected from three
694 independent experiments. Two varicosities were identified per image.

695

696 **RNA-seq mining and data analysis.** All RNA sequencing data was accessed via the Gene Expression
697 Omnibus (GEO) under the following accession numbers: GSE108020, GSE115070, GSE76381, GSE116470,
698 GSE116138. Raw counts were converted to RPKM and quantile normalized using the preprocessCore
699 (3.11) package in R.

700

701 **Statistical Analysis.** Statistical details can be found in the figure legends and were computed with
702 GraphPad Prism 8. When employing one-way ANOVA, Dunnett's post hoc test was used for multiple
703 comparisons. The dSTORM comparisons were normalized to the control sample from the individual
704 imaging session. This was done to control for unavoidable variability in sample preparations and between
705 imaging sessions.

Experiment	Number of sample preparations	Number of dSTORM Images	Number of varicosities (neuron experiments) or cells (CAD cell experiment)
IHC dSTORM NMDA	3	102	4028
CAD Cell D421N	3	55	80
Membrane Potential	3	108	471
NMDA and VGCC	3	188	841
Haloperidol and VGCC	3	180	840
BAPTA-AM	3	95	208
STX1 NMDA	4	162	678
Clathrin NMDA	3	90	304
PIP2 Haloperidol	3	84	309
PIP2 NMDA	3	88	384
D2 NMDA	3	101	344

D2 Haloperidol	3	90	524

Data Availability. Custom written codes used for the data analysis can be found at: https://github.com/GetherLab/Super-Resolution-Data-Analysis. . The datasets supporting the current study have not been deposited in a public repository because of the file size but are available from the corresponding author on request.

713 **REFERENCES**

714 1 Groc, L. & Choquet, D. Linking glutamate receptor movements and synapse function. *Science*
715 **368** (2020).

716 2 Choquet, D. & Hosy, E. AMPA receptor nanoscale dynamic organization and synaptic plasticities.
717 *Curr Opin Neurobiol* **63**, 137-145 (2020).

718 3 Liu, C. & Kaeser, P. S. Mechanisms and regulation of dopamine release. *Curr Opin Neurobiol* **57**,
719 46-53 (2019).

720 4 Bjorklund, A. & Dunnett, S. B. Dopamine neuron systems in the brain: an update. *Trends*
721 *Neurosci* **30**, 194-202 (2007).

722 5 Tritsch, N. X. & Sabatini, B. L. Dopaminergic modulation of synaptic transmission in cortex and
723 striatum. *Neuron* **76**, 33-50 (2012).

724 6 Descarries, L., Watkins, K. C., Garcia, S., Bosler, O. & Doucet, G. Dual character, asynaptic and
725 synaptic, of the dopamine innervation in adult rat neostriatum: a quantitative autoradiographic
726 and immunocytochemical analysis. *J Comp Neurol* **375**, 167-186 (1996).

727 7 Giguere, N. *et al.* Increased vulnerability of nigral dopamine neurons after expansion of their
728 axonal arborization size through D2 dopamine receptor conditional knockout. *PLoS Genet* **15**,
729 e1008352 (2019).

730 8 Borroto-Escuela, D. O. *et al.* Brain Dopamine Transmission in Health and Parkinson's Disease:
731 Modulation of Synaptic Transmission and Plasticity Through Volume Transmission and
732 Dopamine Heteroreceptors. *Front Synaptic Neurosci* **10**, 20 (2018).

733 9 Kristensen, A. S. *et al.* SLC6 neurotransmitter transporters: structure, function, and regulation.
734 *Pharmacol Rev* **63**, 585-640 (2011).

735 10 Torres, G. E. & Amara, S. G. Glutamate and monoamine transporters: new visions of form and
736 function. *Curr Opin Neurobiol* **17**, 304-312 (2007).

737 11 Bermingham, D. P. & Blakely, R. D. Kinase-dependent Regulation of Monoamine
738 Neurotransmitter Transporters. *Pharmacol Rev* **68**, 888-953 (2016).

739 12 Torres, G. E. The dopamine transporter proteome. *J Neurochem* **97 Suppl 1**, 3-10 (2006).

740 13 Rahbek-Clemmensen, T. *et al.* Super-resolution microscopy reveals functional organization of
741 dopamine transporters into cholesterol and neuronal activity-dependent nanodomains. *Nat*
742 *Commun* **8**, 740 (2017).

743 14 Betzig, E. *et al.* Imaging intracellular fluorescent proteins at nanometer resolution. *Science* **313**,
744 1642-1645 (2006).

745 15 Heilemann, M. *et al.* Subdiffraction-resolution fluorescence imaging with conventional
746 fluorescent probes. *Angew Chem Int Ed Engl* **47**, 6172-6176 (2008).

747 16 Huang, B., Bates, M. & Zhuang, X. Super-resolution fluorescence microscopy. *Annu Rev Biochem*
748 **78**, 993-1016 (2009).

749 17 Tillberg, P. W. *et al.* Protein-retention expansion microscopy of cells and tissues labeled using
750 standard fluorescent proteins and antibodies. *Nat Biotechnol* **34**, 987-992 (2016).

751 18 Truckenbrodt, S., Sommer, C., Rizzoli, S. O. & Danzl, J. G. A practical guide to optimization in X10
752 expansion microscopy. *Nat Protoc* **14**, 832-863 (2019).

753 19 Chen, F., Tillberg, P. W. & Boyden, E. S. Optical imaging. Expansion microscopy. *Science* **347**,
754 543-548 (2015).

755 20 Manley, S. *et al.* High-density mapping of single-molecule trajectories with photoactivated
756 localization microscopy. *Nat Methods* **5**, 155-157 (2008).

757 21 Guthrie, D. A. *et al.* Novel Fluorescent Ligands Enable Single-Molecule Localization Microscopy
758 of the Dopamine Transporter. *ACS Chem Neurosci* **11**, 3288-3300 (2020).

759 22 Baker, S. M., Buckheit, R. W., 3rd & Falk, M. M. Green-to-red photoconvertible fluorescent
760 proteins: tracking cell and protein dynamics on standard wide-field mercury arc-based
761 microscopes. *BMC Cell Biol* **11**, 15 (2010).

762 23 Shivanandan, A., Deschout, H., Scarselli, M. & Radenovic, A. Challenges in quantitative single
763 molecule localization microscopy. *FEBS Lett* **588**, 3595-3602 (2014).

764 24 Ester, M., Kriegel, H.-P., Sander, J. & Xu, X. in *Proc. 2nd International Conference on Knowledge*
765 *Discovery and Data Mining* 226–231 (AAAI Press, 1996).

766 25 Levet, F. *et al.* A tessellation-based colocalization analysis approach for single-molecule
767 localization microscopy. *Nat Commun* **10**, 2379 (2019).

768 26 Ehmann, N. *et al.* Quantitative super-resolution imaging of Bruchpilot distinguishes active zone
769 states. *Nat Commun* **5**, 4650 (2014).

770 27 Siddig, S. *et al.* Super-resolution imaging reveals the nanoscale organization of metabotropic
771 glutamate receptors at presynaptic active zones. *Science Advances* **6**, eaay7193 (2020).

772 28 Baumgart, F. *et al.* Varying label density allows artifact-free analysis of membrane-protein
773 nanoclusters. *Nat Methods* **13**, 661-664 (2016).

774 29 Newman, A. H. *et al.* Translating the atypical dopamine uptake inhibitor hypothesis toward
775 therapeutics for treatment of psychostimulant use disorders. *Neuropsychopharmacology* **44**,
776 1435-1444 (2019).

777 30 Beuming, T. *et al.* The binding sites for cocaine and dopamine in the dopamine transporter
778 overlap. *Nat Neurosci* **11**, 780-789 (2008).

779 31 Lebowitz, J. J. & Khoshbouei, H. Heterogeneity of dopamine release sites in health and
780 degeneration. *Neurobiol Dis* **134**, 104633 (2020).

781 32 Herborg, F., Andreassen, T. F., Berlin, F., Loland, C. J. & Gether, U. Neuropsychiatric disease-
782 associated genetic variants of the dopamine transporter display heterogeneous molecular
783 phenotypes. *J Biol Chem* **293**, 7250-7262 (2018).

784 33 Salamone, A. *et al.* Prolonged nicotine exposure down-regulates presynaptic NMDA receptors in
785 dopaminergic terminals of the rat nucleus accumbens. *Neuropharmacology* **79**, 488-497 (2014).

786 34 Lin, C.-W. *et al.* Genetically increased cell-intrinsic excitability enhances neuronal integration
787 into adult brain circuits. *Neuron* **65**, 32-39 (2010).

788 35 Xue, M., Atallah, B. V. & Scanziani, M. Equalizing excitation-inhibition ratios across visual cortical
789 neurons. *Nature* **511**, 596-600 (2014).

790 36 Rayport, S. *et al.* Identified postnatal mesolimbic dopamine neurons in culture: morphology and
791 electrophysiology. *J Neurosci* **12**, 4264-4280 (1992).

792 37 Turner, T. J., Adams, M. E. & Dunlap, K. Multiple Ca2+ channel types coexist to regulate
793 synaptosomal neurotransmitter release. *Proceedings of the National Academy of Sciences of the*
794 *United States of America* **90**, 9518-9522 (1993).

795 38 Beaulieu, J. M. & Gainetdinov, R. R. The physiology, signaling, and pharmacology of dopamine
796 receptors. *Pharmacol Rev* **63**, 182-217 (2011).

797 39 Prasad, B. M. & Amara, S. G. The dopamine transporter in mesencephalic cultures is refractory
798 to physiological changes in membrane voltage. *J Neurosci* **21**, 7561-7567 (2001).

799 40 Strange, P. G. Antipsychotic drug action: antagonism, inverse agonism or partial agonism. *Trends*
800 *Pharmacol Sci* **29**, 314-321 (2008).

801 41 Belovich, A. N. *et al.* A network of phosphatidylinositol (4,5)-bisphosphate (PIP2) binding sites
802 on the dopamine transporter regulates amphetamine behavior in Drosophila Melanogaster.
803 *Molecular Psychiatry* (2019).

804 42 van den Bogaart, G. *et al.* Membrane protein sequestering by ionic protein-lipid interactions.
805 *Nature* **479**, 552-555 (2011).

806 43 Maxfield, F. R. & McGraw, T. E. Endocytic recycling. *Nature Reviews Molecular Cell Biology* **5**,
807 121-132 (2004).

808 44 Li, Y. M. *et al.* Real-time 3D single-molecule localization using experimental point spread
809 functions. *Nat. Methods* **15**, 367-+ (2018).

810 45 Padmanabhan, P. *et al.* Need for speed: Super-resolving the dynamic nanoclustering of syntaxin-
811 1 at exocytic fusion sites. *Neuropharmacology* **169** (2020).

812 46 Binda, F. *et al.* Syntaxin 1A interaction with the dopamine transporter promotes amphetamine-
813 induced dopamine efflux. *Mol Pharmacol* **74**, 1101-1108 (2008).

814 47 Goncalves, J. *et al.* Nanoscale co-organization and coactivation of AMPAR, NMDAR, and mGluR
815 at excitatory synapses. *Proc Natl Acad Sci U S A* **117**, 14503-14511 (2020).

816 48 Das, A. K. *et al.* Dopamine transporter forms stable dimers in the live cell plasma membrane in a
817 phosphatidylinositol 4,5-bisphosphate-independent manner. *J Biol Chem* **294**, 5632-5642
818 (2019).

819 49 Pereira, D. B. *et al.* Fluorescent false neurotransmitter reveals functionally silent dopamine
820 vesicle clusters in the striatum. *Nat Neurosci* **19**, 578-586 (2016).

821 50 McLaughlin, S. & Murray, D. Plasma membrane phosphoinositide organization by protein
822 electrostatics. *Nature* **438** (2005).

823 51 Hamilton, P. J. *et al.* PIP2 regulates psychostimulant behaviors through its interaction with a
824 membrane protein. *Nat Chem Biol* **10**, 582-589 (2014).

825 52 Suh, B. C. & Hille, B. PIP2 is a necessary cofactor for ion channel function: how and why? *Annu*
826 *Rev Biophys* **37**, 175-195 (2008).

827 53 Robertson, S. D., Matthies, H. J. & Galli, A. A closer look at amphetamine-induced reverse
828 transport and trafficking of the dopamine and norepinephrine transporters. *Mol Neurobiol* **39**,
829 73-80 (2009).

830 54 Hong, W. C. & Amara, S. G. Membrane cholesterol modulates the outward facing conformation
831 of the dopamine transporter and alters cocaine binding. *J Biol Chem* **285**, 32616-32626 (2010).

832 55 Carquin, M., D'Auria, L., Pollet, H., Bongarzone, E. R. & Tyteca, D. Recent progress on lipid lateral
833 heterogeneity in plasma membranes: From rafts to submicrometric domains. *Progress in Lipid*
834 *Research* **62**, 1-24 (2016).

835 56 Thal, L. B. *et al.* Single Quantum Dot Imaging Reveals PKCbeta-Dependent Alterations in
836 Membrane Diffusion and Clustering of an Attention-Deficit Hyperactivity
837 Disorder/Autism/Bipolar Disorder-Associated Dopamine Transporter Variant. *ACS Chem*
838 *Neurosci* **10**, 460-471 (2019).

839 57 Lee, F. J. *et al.* Dopamine transporter cell surface localization facilitated by a direct interaction
840 with the dopamine D2 receptor. *Embo J* **26**, 2127-2136 (2007).

841 58 Bolan, E. A. *et al.* D2 receptors regulate dopamine transporter function via an extracellular
842 signal-regulated kinases 1 and 2-dependent and phosphoinositide 3 kinase-independent
843 mechanism. *Mol Pharmacol* **71**, 1222-1232 (2007).

844 59 Zapata, A. *et al.* Regulation of dopamine transporter function and cell surface expression by D3
845 dopamine receptors. *J Biol Chem* **282**, 35842-35854 (2007).

846 60 Maidorn, M., Olichon, A., Rizzoli, S. O. & Opazo, F. Nanobodies reveal an extra-synaptic
847 population of SNAP-25 and Syntaxin 1A in hippocampal neurons. *Mabs* **11**, 305-321 (2019).

848 61 Loland, C. J., Granas, C., Javitch, J. A. & Gether, U. Identification of intracellular residues in the
849 dopamine transporter critical for regulation of transporter conformation and cocaine binding. *J*
850 *Biol Chem* **279**, 3228-3238. (2004).

851 62 Klewe, I. V. *et al.* Recruitment of beta-arrestin2 to the dopamine D2 receptor: insights into anti-
852 psychotic and anti-parkinsonian drug receptor signaling. *Neuropharmacology* **54**, 1215-1222
853 (2008).

854 63 Jeong, J. Y. *et al.* One-step sequence- and ligation-independent cloning as a rapid and versatile
855 cloning method for functional genomics studies. *Appl Environ Microbiol* **78**, 5440-5443 (2012).

856 64 Matsui, R., Tanabe, Y. & Watanabe, D. Avian adeno-associated virus vector efficiently
857 transduces neurons in the embryonic and post-embryonic chicken brain. *PLoS One* **7**, e48730
858 (2012).

859 65 Piedra, J. *et al.* Development of a rapid, robust, and universal picogreen-based method to titer
860 adeno-associated vectors. *Hum Gene Ther Methods* **26**, 35-42 (2015).

861 66 Underhill, S. M. *et al.* Amphetamine modulates excitatory neurotransmission through
862 endocytosis of the glutamate transporter EAAT3 in dopamine neurons. *Neuron* **83**, 404-416
863 (2014).

864 67 Ovesny, M., Krizek, P., Borkovec, J., Svindrych, Z. & Hagen, G. M. ThunderSTORM: a
865 comprehensive ImageJ plug-in for PALM and STORM data analysis and super-resolution imaging.
866 *Bioinformatics* **30**, 2389-2390 (2014).

867 68 Wang, Y. *et al.* Localization events-based sample drift correction for localization microscopy
868 with redundant cross-correlation algorithm. *Opt Express* **22**, 15982-15991 (2014).

869 69 Qi, Y., Wang, J. K., McMillian, M. & Chikaraishi, D. M. Characterization of a CNS cell line, CAD, in
870 which morphological differentiation is initiated by serum deprivation. *J Neurosci* **17**, 1217-1225
871 (1997).

872 70 Turkowyd, B. *et al.* Establishing Live-Cell Single-Molecule Localization Microscopy Imaging and
873 Single-Particle Tracking in the Archaeon Haloferax volcanii. *Front Microbiol* **11**, 583010 (2020).

874

875

Acknowledgement

We thank Ralph Götz for support with expansion microscopy. The work was supported by the Lundbeck Foundation grants R266-2017-4331 (UG), R276-2018-792 (UG), R230-2016-3154 (M.D.L.), R181-2014-3090 (FH), R303-2018-3540 (F.H.) and R231-2016-2481-5 (ATS), Independent Research Fund Denmark – Medical Sciences (U.G. 7016-00325B), and the NIDA-Intramural Research Program Z1A DA000610 (AHN and DAG).

Author contributions

M.D.L. performed all the experiments and wrote the analyses not hereafter mentioned; A.L.E. devised the cluster size algorithm and identified mRNA expression data; A.T.S. performed electrophysiology and generated the construct encoding Cre recombinase under control of a truncated TH promotor; N.O.H. performed the D421N CAD cell experiments; S.H.J. cloned Kir2.1 and mNaChBac plasmids and made non-commercially available viruses; D.A.G. and A.H.N. invented and synthesized the fluorescent cocaine analogs; J.F.S. optimized the DA neuron culture protocol; M.D.L., F.H., and U.G. conceptualized the study, designed the research and interpreted data; U.G., F.H., M.S., and C.W. supervised the research. M.D.L., U.G., and F.H. wrote the paper with contributions from M.S. and all the other authors.

Competing interests

The authors declare no competing financial interests.

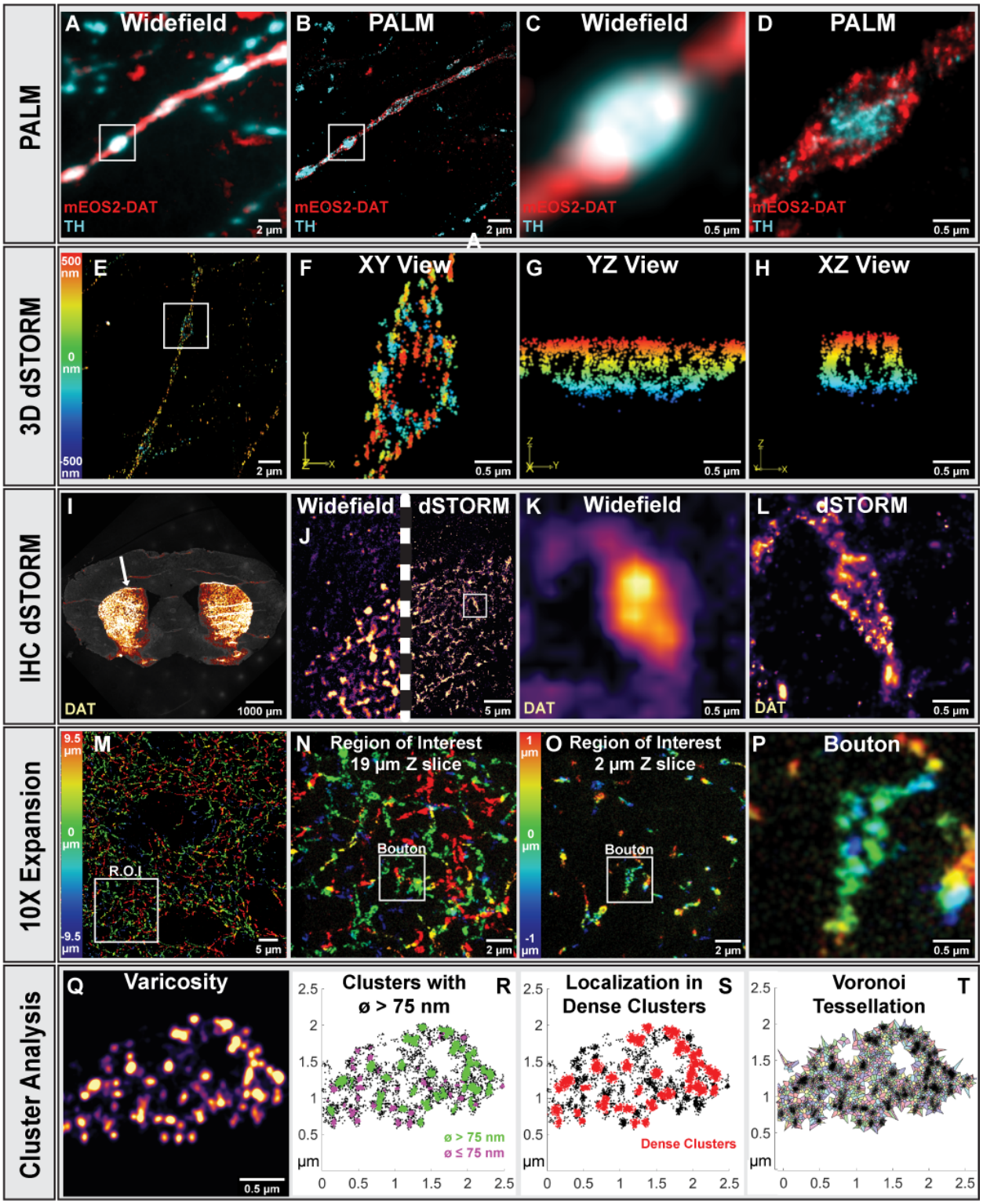

Fig. 1. DAT shows nanodomain distribution in cultured neurons and striatal slices. (A-D) Visualization of mEOS2-DAT overexpressed in cultured DA neurons. Endogenous TH was labeled to identify DA neurons. (A, C) Widefield images (C is boxed region in A). (B, D) PALM/dSTORM images (D is boxed region in B). (E-H) 3D dSTORM image of DAT in DA neurons (color-coded based on depth). (E) Neuronal extension. (F)

905 Varicosity (boxed region in E) (XY perspective). (G) YZ perspective. (H) XZ perspective. (I-L) Mouse brain
906 coronal section immunolabeled for DAT. (I) brain slice with striatal DAT staining. (J) Comparison of
907 widefield with dSTORM. (K) Widefield view of varicosity. (L) dSTORM image. (M-P) 10 x Expansion
908 Microscopy (ExM) on mouse striatal slice immunolabeled for DAT. N shows region of interest (R.O.I.) in
909 M with the full 19 µM Z slice (color-coded based on depth); O is R.O.I. in M with just 2 µM of the Z axis.
910 (P) Single varicosity identified in O. (Q-T) Cluster metrics demonstrated on a varicosity immunolabeled for
911 DAT. Q, dSTORM of single varicosity. (R, S) Identification of clusters by DBSCAN; clusters with diameter
912 >75 nm in green, clusters <75 nm in magenta; dense clusters (>80 localizations within a radius of 50 nm)
913 in red. (T) DAT localizations segmented by Voronoi tessellation.
914
915
916

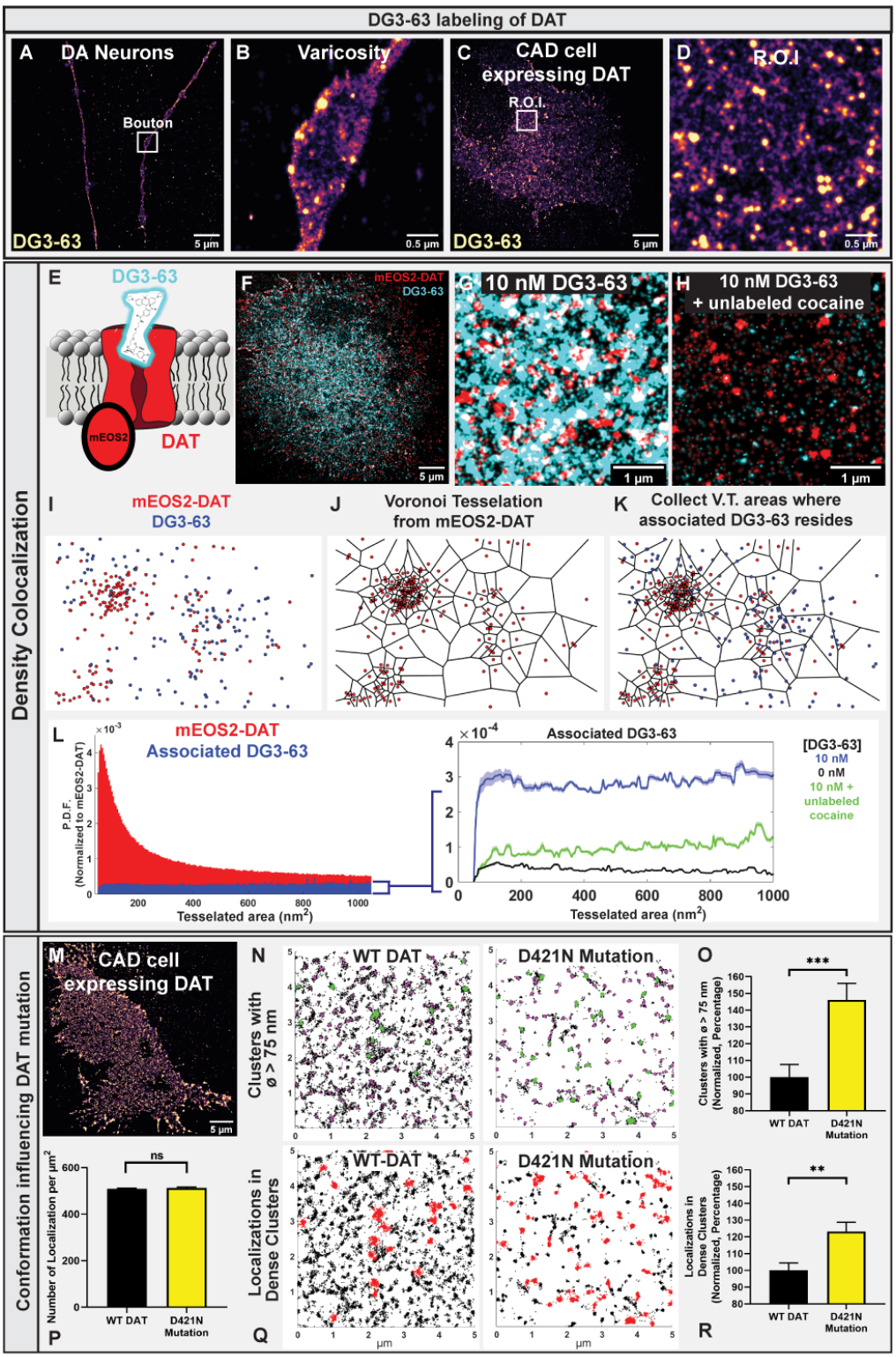

Fig. 2. Nanodomain localized DAT is preferentially in an inward-facing conformation. (A-D) dSTORM on DA neurons and DAT expressing CAD cells labeled with the fluorescent cocaine analogue DG3-63 (10 nM). (A) Axonal extension. (B) varicosity (box in A). (C) CAD cell. (D) R.O.I. from C. (E-H) The density-based association of DG3-63 to mEOS2-DAT. (E) Cartoon of labeling strategy. (F) dSTORM/PALM image of CAD

923 cell expressing mEOS2-DAT (red) and labeled with DG3-63 (10 nM)(blue). (G) Close-up dSTORM/PALM
924 image of CAD cell expressing mEOS2-DAT (red) and labeled with DG3-63 (10 nM) (blue). (H) The DG3-63
925 signal is blocked by 100 µM cocaine. (I-K) Voronoi tessellation based colocalization algorithm. Tessellation
926 is performed on the mEOS2-DAT data and areas are marked for when the mEOS2-DAT localization has a
927 DG3-63 localization within 25 nm distance. (L) Left, Total mEOS2-DAT Voronoi tesselated area distribution
928 (red) (probability density function (P.D.F.) and tessellated areas of mEOS2-DAT associated with DG3-63
929 (blue). Right, tessellated areas for mEOS2-DAT associated with DG3-63 (blue) compared to that associated
930 in presence of saturating cocaine. (M-O) TIRF/dSTORM of WT DAT and inward-facing mutant (D421N).
931 (M) Example image of DAT expressed in CAD cells. (N) Example images of clusters with diameter >75 nm
932 (green) in WT DAT and D421N Dcells. (O) Normalized fraction of clusters with diameter >75 nm (in %),
933 means ± S.E., from 38 WT DAT cells and 42 D421N cells, 3 transfections, ***p<0.001, unpaired t-test.
934 (P-O)dSTORM of WT DAT and inward-facing mutant (D421N). (P) Number of localizations per μm^2 forWT
935 DAT and D421N, means ± S.E., unpaired t test, p= 0.4. (Q) Example image of dense clusters (red) of WT
936 DAT and D421N (radius 100 nm, >100 localizations). (R) Fraction of localizations in dense clusters (in % of
937 WT DAT), means ± S.E., from 38 WT DAT cells and 42 D421N cells, 3 transfections, **p<0.01, unpaired t-
938 test.
939

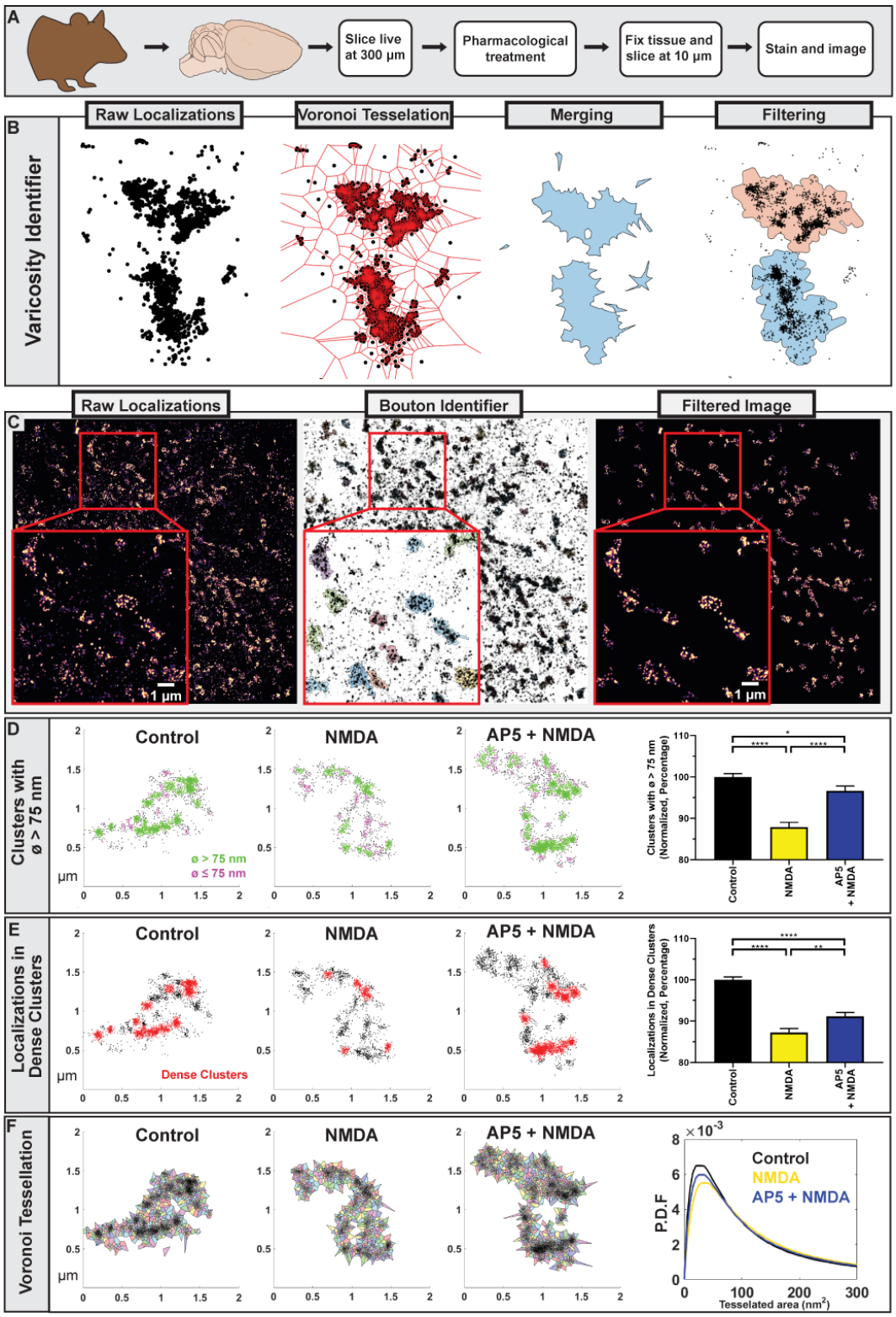

Fig. 3. NMDA receptor activation declusters DAT in mouse brain slices. (A) Workflow diagram. (B) Data processing steps to isolate single varicosities from dSTORM images (see Methods). (C) Representative DAT dSTORM image before, during, and after varicosity identification. (D)Example varicosity from control,

945 NMDA, and AP5 + NMDA treated slices (clusters with diameter >75 nm in green, clusters <75 nm in
946 magenta). Right, Normalized fraction of DAT clusters >75 nm (in %), means ± S.E., from 3 experiments
947 with analysis of 1793 control, 1102 NMDA and 1033 NMDA + AP5 varicosities; one-way ANOVA,
948 ****p<0.0001, *p<0.05. (E) Example varicosity from control, NMDA (20 µM), and AP5 + NMDA (20 µM)
949 treated slices (dense clusters in red, >80 localizations, radius 50 nm). Right, Normalized fraction of DAT
950 localizations in dense clusters (in %), means ± S.E.; one-way ANOVA, ****p<0.0001, ***p<0.001,
951 **p<0.01. (F) The probability density functions (P.D.F.) for the Voronoi tessellated areas averaged by
952 varicosity.
953

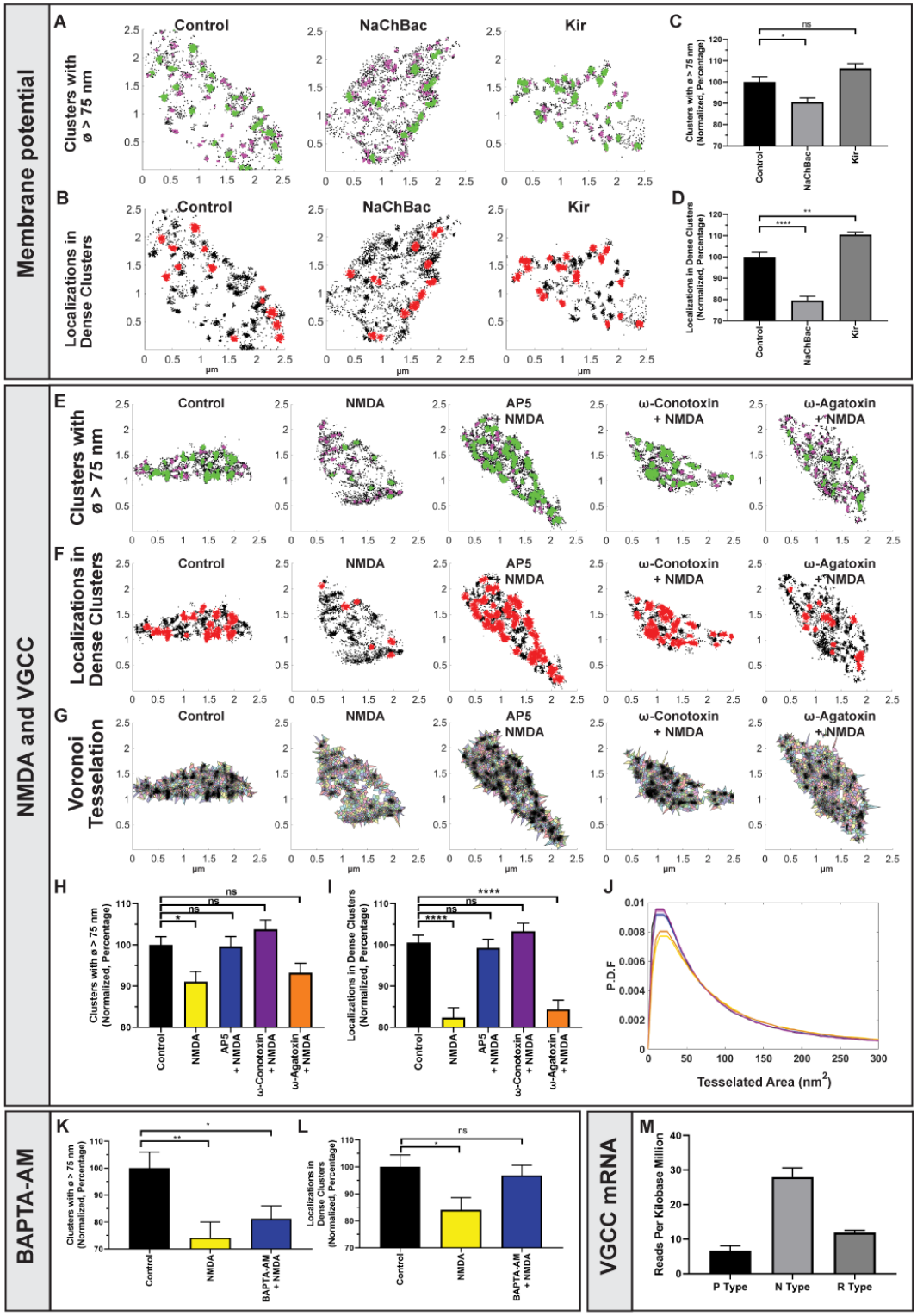

Fig. 4. DAT nanodomain localization is regulated by neuronal activity in a Ca^{2+} dependent manner. (A-D) Expression of the Na^+ channel mNaChBac or the K^+ channel Kir2.1 in DA neurons. Example varicosities from DAT dSTORM of control, mNaChBac or Kir2.1 expressing DA neurons. (A) DAT clusters with diameter

959 >75 nm in green, clusters <75 nm in magenta. (B) Dense DAT clusters in red (>80 localizations, radius 50
960 nm). (C) Normalized fraction of clusters >75 nm (in %). (D) Normalized fraction of DAT localizations in
961 dense clusters (in %), means ± S.E.; data from 3 cultures and 80 control, 230 mNaChBac and 161 Kir2.1
962 varicosities; one-way ANOVA, ****p<0.0001, **p<0.01, *p<0.05, n.s., not significant. (E-J) The effect of
963 NMDA on DAT nanodomains is blocked by the N-type VGCC blocker ω-conotoxin. Example varicosities
964 from dSTORM of DA neurons subject to 5 min treatment with vehicle, NMDA (20 µM), AP5 (100 µM) +
965 NMDA (20 µM), ω-Conotoxin (1 µM) + NMDA (20 µM) or ω-Agatoxin (1 µM) + NMDA (20 µM). (E) DAT
966 clusters with diameter >75 nm in green, clusters <75 nm in magenta. (F) Dense DAT clusters in red (>80
967 localizations, radius 50 nm). (G) localizations segmented by Voronoi tessellation. (H, I) Normalized fraction
968 of DAT clusters >75 nm (in %) (H) and normalized fraction of DAT localizations in dense clusters (in %) (I),
969 means ± S.E.; one-way ANOVA, ****p< <0.0001, *p<0.05, n.s., not significant. (J) Probability density
970 functions (P.D.F.) (curves color-coded as in the bar diagrams) for the Voronoi tessellated areas averaged
971 by varicosity. Data are from 3 cultures and 190 control, 147 NMDA, 170 AP5, 180 ω-Conotoxin and 154
972 ω-Agatoxin varicosities. (K, L) Pretreatment (30 in) with BAPTA-AM inhibits the dispersing effect of NMDA
973 on DAT nanodomains. (K) Normalized fraction of DAT clusters >75 nm (in %) and (L) normalized fraction
974 of DAT localizations in dense clusters (in %) for control, NMDA (20 µM) and NMDA (20 µM) + BAPTA-AM
975 (25 µM), means ± S.E.; data from 3 cultures and includes analysis of 66 control, 72 NMDA and 70 BAPTA-
976 AM + NMDA varicosities, one-way ANOVA, **p<0.01, *p<0.05, n.s., not significant. (M) mRNA expression
977 for P, R, and N-type VGCC in DA neurons based on single cell RNAseq data (see Methods).
978
979

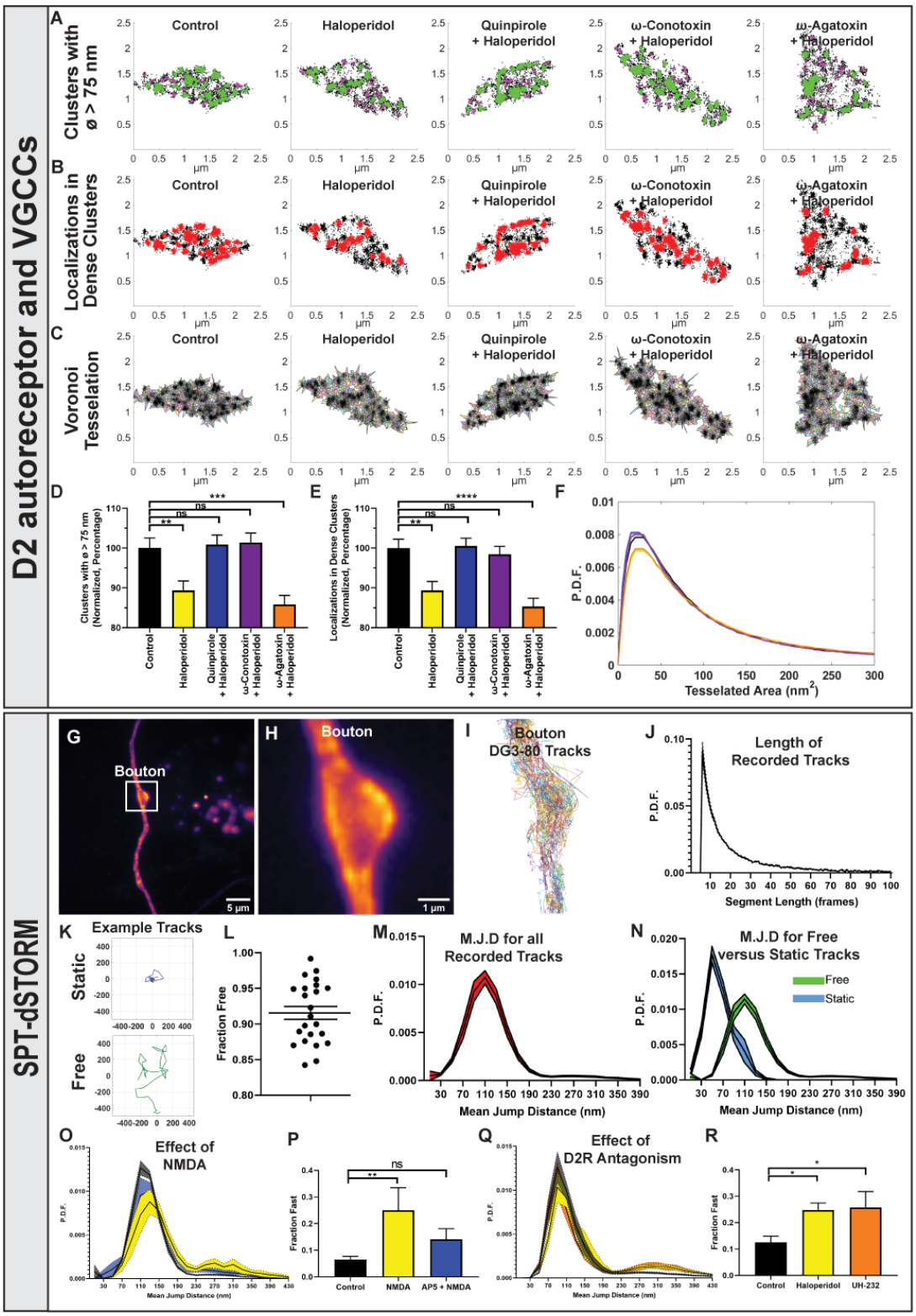

Fig. 5. DAT nanodomain localization is regulated by the D2R and involves changes in lateral mobility. A-F) Dispersal of DAT nanodomains is promoted by the D2R antagonist haloperidol and blocked by the agonist quinpirole and by the N-type VGCC blocker ω-conotoxin. Example varicosities from dSTORM of

985 DA neurons subject 5 min treatment with haloperidol (10 nM), haloperidol (10 nM) + quinpirole (50 µM),
986 haloperidol (10 nM) + ω-conotoxin (1 µM) or haloperidol (10 nM) + ω-agatoxin (1 µM). (A) DAT clusters
987 with diameter >75 nm in green, clusters <75 nm in magenta. (B) Dense DAT clusters in red (>80
988 localizations, radius 50 nm). (C) localizations segmented by Voronoi tessellation. (D, E) Normalized
989 fraction of DAT clusters >75 nm (in %) (D) and normalized fraction of DAT localizations in dense clusters
990 (in %) (E), means ± S.E.; one-way ANOVA, ****p<0.0001, ***p<0.001, **p<0.01, *p<0.05, n.s., not
991 significant. (F) Probability density functions (P.D.F.) (curves color-coded as in the bar diagrams) for the
992 Voronoi tessellated areas averaged by varicosity. Probability density functions (P.D.F.) (curves color-
993 coded as in the bar diagrams) for the Voronoi tessellated areas averaged by varicosity. Data are from 3
994 cultures and 153 control, 166 haloperidol, 167 quinpirole, 178 ω-conotoxin and 176 ω-agatoxin
995 varicosities. (G-R) Single particle tracking dSTORM (SPT-dSTORM) identifies changes in DAT mobility in
996 response to NMDA and D2R antagonism. (G) Example live dSTORM images of DA neurons labeled with
997 the fluorescent cocaine analogue, DG3-80. (H) Boxed region in B. (I) Detected tracks and (J) Distribution
998 of segment lengths in varicosity from control SPT-dSTORM experiment (16 ms frame rate). (K) Example
999 traces of a confined and an unconstrained freely moving particle (DG3-80 labeled DAT). (L) Fraction of
1000 unconstrained tracks out of the total number of tracks. Data are means of 23 tracks ± S.E. (M) Probability
1001 Density Function (P.D.F.) for total mean jump distances (M.J. D) (i.e. the distance an individual
1002 molecule/particle has traveled between each image) for control experiments. (N) P.D.F. when separated
1003 into static and freely moving particles. Among the freely moving particles, some moved very fast with
1004 M.J.D. of 200-350 nm. (O) NMDA (20 µM, 5 min) increases population of DAT molecules with M.J.D. > 200
1005 nm, which is blunted by AP5 (100 µM). (P) Fraction of fast moving particles (> 200 nm), means ± S.E., data
1006 from 13 control, 4 NMDA and 5 NMDA+AP5 experiments; (Q, R) The D2R antagonists haloperidol (10 nM,
1007 5 min) and UH-232 (1 µM) increase the population of DAT molecules with M.J.D. > 200 nm > 200 nm; M,
1008 Fraction of fast moving particles (> 200 nm), means ± S.E., data are from 10 control, 6 haloperidol and 5
1009 UH-232 experiments; one-way ANOVA, *p<0.05; **p<0.01, n.s., not significant.
1010
1011

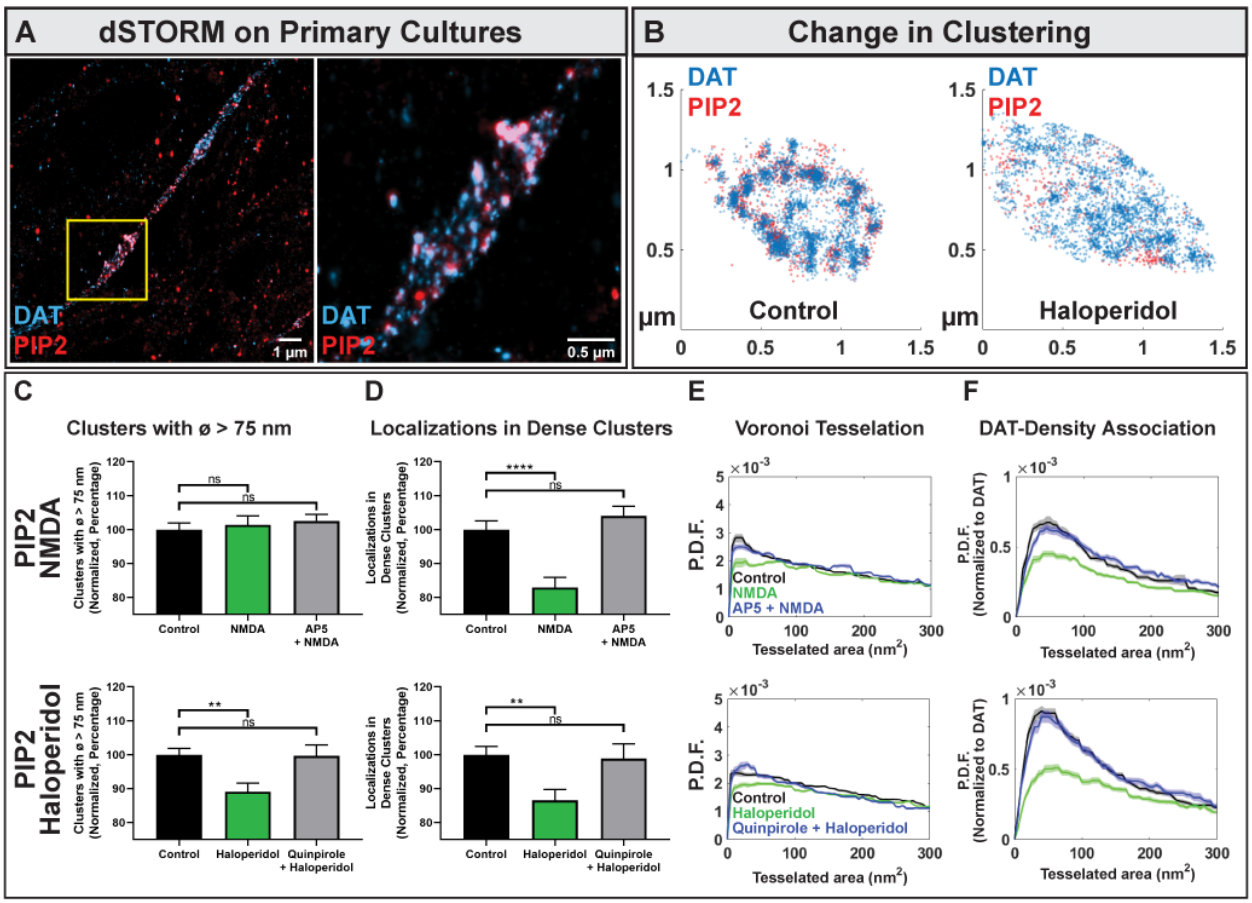

Fig. 6. DAT nanodomains overlap with PIP2 nanodomains. Example dual-color dSTORM images of phosphatidylinositol 4,5-bisphosphate (PIP2) (red, CF568) and DAT (blue, Alexa647) in a neuronal extension from cultured DA neurons (left) with close-up image of varicosity (right) corresponding to boxed region in the left image. Example dual-color dSTORM images of varicosities from DA neurons showing localizations for PIP2 (red) and DAT (blue). Left, Control; Right, neurons exposed to haloperidol (10 nM, 5 min). (C-F) Effect of NMDA and haloperidol on PIP2 clustering. Upper panels, Control, NMDA (20 µM) and NMDA (20 µM) + AP5 (100 µM); Lower panels; Control, haloperidol (10 nM) and haloperidol (10 nM) + quinpirole (50 µM). (C) Normalized fraction of PIP2 localizations in large clusters (>75 nm in diameter) (in %) and (D), normalized fraction of PIP2 localizations in dense clusters (>80 localizations, radius 50 nm) (in %), means ±S.E., one-way ANOVA, ****p<0.0001, **p<0.01, n.s., not significant. (E) Probability density functions (P.D.F.) (color-coded as in the bar diagrams) for the Voronoi tessellated areas averaged by varicosity. (F) Probability density functions (P.D.F.) (color-coded as in the bar diagrams) of the association of PIP2 with DAT clusters determined by Voronoi tessellation-based association (see Fig. 2) showing strong association PIP2 with DAT. Data are from 3 cultures and 137 control, 126 NMDA, 121 NMDA + AP5 varicosities; and 140 control, 102 haloperidol, 67 haloperidol + quinpirole varicosities,

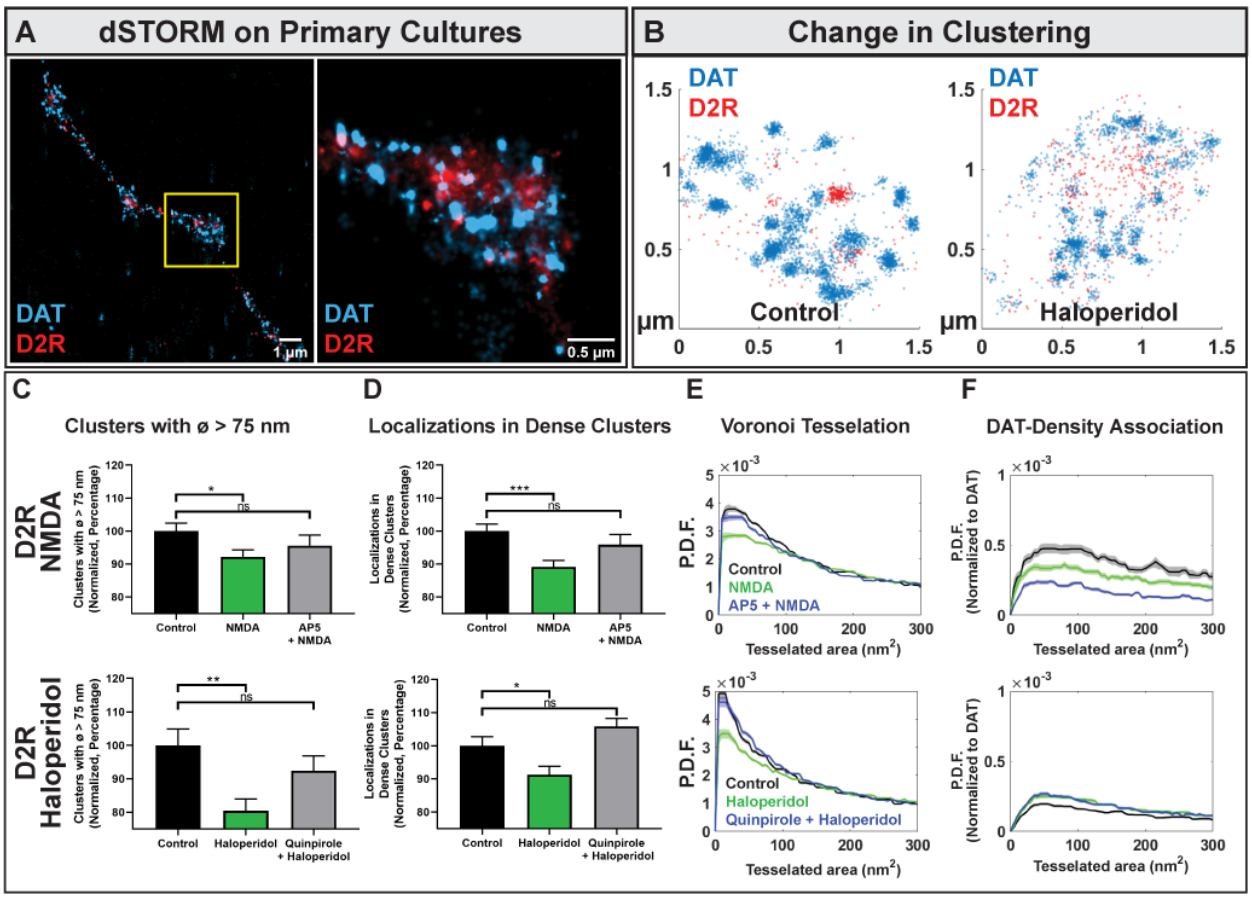

Fig. 7. The D2R is also distributed into nanodomains. (A) Example dual-color dSTORM images of the D2R (red, CF568) and DAT (blue, Alexa647) in DA neuronal extension (left) with close-up image of varicosity (right) corresponding to boxed region in the left image. (B) Example dual color dSTORM images of varicosities from DA neurons showing localizations for D2R (red) and DAT (blue). Left, Control; Right, neurons exposed to haloperidol (10 nM, 5 min). (C-F) Effect of NMDA and haloperidol on D2R clustering. Upper panels, Control, NMDA (20 µM) and NMDA (20 µM) + AP5 (100 µM); Lower panels; Control, haloperidol (10 nM) and haloperidol (10 nM) + quinpirole (50 µM). (C) Normalized fraction of D2R localizations in large clusters (>75 nm in diameter) (in %) and (D), normalized fraction of D2R localizations in dense clusters (>80 localizations, radius 50 nm) (in %), means ±S.E., one-way ANOVA, ***p<0.001, **p<0.01, *p<0.05, n.s., not significant. (E) Probability density functions (P.D.F.) (color-coded as in the bar diagrams) for the Voronoi tessellated areas averaged by varicosity. (F) Probability density functions (P.D.F.) (color-coded as in the bar diagrams) of the association of D2R with DAT clusters determined by Voronoi tessellation-based association (see Fig. 2). Data are from 3 cultures and data from 3 cultures and 112 control, 157 NMDA, 75 NMDA + AP5; and 179 control, 195 haloperidol and 150 quinpirole varicosities.